Chem Soc Rev

Symmetry Breaking in Molecular Ferroelectrics

Journal:	*Chemical Society Reviews*
Manuscript ID	CS-SYN-04-2015-000308.R3
Article Type:	Review Article
Date Submitted by the Author:	18-Mar-2016
Complete List of Authors:	Shi, Ping-Ping; Southeast University, Ordered Matter Science Research Center Tang, Yuan-Yuan; Ordered Matter Science Research Center, Southeast University Li, Peng-fei; Ordered Matter Science Research Center, Southeast University Liao, Wei-Qiang ; Ordered Matter Science Research Center, Southeast University Wang, Zhong-Xia; Ordered Matter Science Research Center, Southeast University Ye, Qiong; Ordered Matter Science Research Center, Southeast University Xiong, Rengen; Southeast University, Ordered Matter Science Research Center

Symmetry breaking in molecular ferroelectrics

*Ping-Ping Shi, Yuan-Yuan Tang, Peng-Fei Li, Wei-Qiang Liao, Zhong-Xia Wang, Qiong Ye and Ren-Gen Xiong**

Ordered Matter Science Research Center, Southeast University, Nanjing 211189, P. R. China. E-mail: xiongrg@seu.edu.cn

The table of contents entry

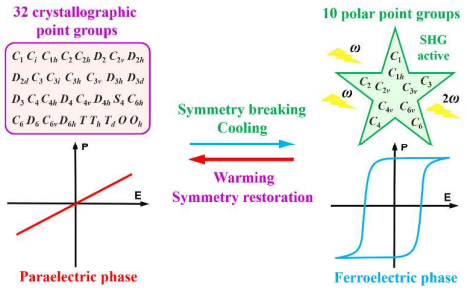

Symmetry breaking occurs between the high-temperature high-symmetry paraelectric phase and the low-temperature low-symmetry ferroelectric phase along with decreased symmetry elements, obeying the Curie symmetry principle and relating to the ferroelectricity.

ABSTRACT:

Ferroelectrics are inseparable from the symmetry breaking. Accompanying the paraelectric-to-ferroelectric phase transition, the paraelectric phase adopting one of the 32 crystallographic point groups is broken to its subgroup belonging to one of the 10 ferroelectric point groups, *i.e.* C_1, C_2, C_{1h}, C_{2v}, C_4, C_{4v}, C_3, C_{3v}, C_6 and C_{6v}. The symmetry breaking is captured by the order parameter called spontaneous polarization, whose switching under an external electric field results in a typical ferroelectric hysteresis loop. In addition, the responses of spontaneous polarization to the other external excitations are also related to a number of physical effects like second-harmonic generation, piezoelectricity, pyroelectricity and dielectric property. Based on these, this review gives the recent development of the molecular ferroelectrics since 2011 and focuses on the relationship between symmetry breaking and ferroelectricity, offering ideas for exploring high-performance molecular ferroelectrics.

1. Introduction

As one of the most important concepts in the fields of materials science and solid-state physics, symmetry plays a crucial role in constructing the structure−property relationships.[1–3] It is simply defined as the physical or mathematical feature of a system which remains constant under a specific group of transformations. These transformations or symmetry operations like translation, inversion, reflection and rotation constitute various symmetry groups. In crystallography, there are 32 point groups and 230 space groups describing the macroscopic and microscopic symmetries of crystal structures, respectively.[4,5] Particularly, the spatial-inversion symmetry indicating the immutability under the inverted spatial coordinates is of paramount significance to the classification of crystals.[6] Among the 32 point groups, 11 centrosymmetric classes have spatial-inversion symmetry, while the remaining 21 noncentrosymmetric ones do not. Actually, the lack of spatial-inversion symmetry is important for many physical systems, especially for ferroelectrics.[7,8]

Ferroelectrics, as an important type of primary ferroic materials, are pyroelectrics in which the direction of the spontaneous polarization (P_s) can be reversed or reoriented by the applied electric field ($\boldsymbol{E}$).[9–11] A characteristic feature of them concerns the transition from a high-temperature high-symmetry paraelectric phase (though there are a few exceptions) to a low-temperature low-symmetry ferroelectric phase in the vicinity of the Curie temperature (T_c).[12–14] Such a paraelectric-to-ferroelectric phase transition normally leads to a small structural distortion but a notable symmetry change. The phenomenon that some symmetry elements of the paraelectric phase are absent in the ferroelectric phase is named as symmetry breaking. Accompanying the symmetry-breaking phase transition, the P_s emerges in the more ordered ferroelectric phase, whereas in the more disordered paraelectric phase the P_s

vanishes. So, being regarded as the ferroelectric order parameter, P_s is used to measure the degree of order and capture the symmetry breaking. The spontaneous switching of P_s will give rise to long range order, ferroelectric domains and the unique hysteretic behavior, affording ferroelectrics an extensive range of technological utilizations in nonvolatile memories, piezoelectric sensors, capacitors, nonlinear optical devices, *etc*.[15–17] Since Rochelle salt (potassium sodium tartrate tetrahydrate, $[KNaC_4H_4O_6](4H_2O)$) was discovered as the first ferroelectric crystal by Valasek in 1920,[18] a great deal of effort has been put into the exploration of ferroelectric materials.[19–21] And, molecular ferroelectrics have been the focus of current researches, by virtue of their various advantages as mechanical flexibility, light weight, structural tunability and multifunctionality. However, the total amount of new molecular ferroelectrics is minimal. Consequently, the toughest issue currently challenging researchers is how to filter ferroelectrics from the numerous crystalline materials more effectively, for the sake of extending the family of ferroelectrics and thereby understanding the ferroelectricity thoroughly. From that perspective, information on symmetry breaking appears to be urgent and important, which is vital to the generation of ferroelectricity.

The relationships between macroscopic symmetries and macroscopic physical properties of crystals are governed by the Neumann's principle that states: the symmetry of any physical property of a crystal must include all the symmetry elements of the point group of the crystal. Normally, the physical properties of crystals, such as the dielectric, pyroelectric, piezoelectric and nonlinear optical properties, are anisotropic and expressed by the property tensors ranging in rank from one to four. According to the Neumann's principle, whether a crystal exhibits a certain physical property or not depends on whether the property tensor keeps fixed under all

the symmetry operations of the point group. Therefore, a given physical property as a matter of course can be employed to identify the crystal symmetry, and conversely, a known crystal symmetry is useful in predicting the physical property.[22,23] Take pyroelectricity for an example, it is defined as the linear relationship between the temperature difference (ΔT) and the change in the induced polarization vector (ΔP_i), *i.e.* $\Delta P_i = p_i \Delta T$, ($i$ = 1, 2, 3), where p_i is the pyroelectric coefficient which acts as a first rank polar tensor. For the 11 centrosymmetric point groups, the absence of p_i can be easily deduced by using the Neumann's principle.[24] And the same is true for the 11 noncentrosymmetric-nonpolar point groups.[25] Consequently, pyroelectricity occurs only in the 10 polar point groups with an unique rotation axis, no inversion center and no mirror plane perpendicular to the rotation axis, that is, 1 (C_1), 2 (C_2), *m* (C_{1h}), *mm*2 (C_{2v}), 4 (C_4), 4*mm* (C_{4v}), 3 (C_3), 3*m* (C_{3v}), 6 (C_6) and 6*mm* (C_{6v}).

On account of the fact that ferroelectrics are a subgroup of pyroelectrics, the ferroelectric phase must adopt one of the 10 polar point groups consisting of 68 polar space groups (as summarized in Tab. 1), requiring the broken spatial-inversion symmetry. By comparison, the paraelectric phase may belong to any of the 32 crystallographic point groups. In the light of the Curie symmetry principle, the symmetry group of the low-temperature ferroelectric phase should be a maximal subgroup of the high-temperature paraelectric symmetry group along the direction of the P_s. Based on this group-to-subgroup relationship, there are 88 species of paraelectric-to-ferroelectric phase transitions given by Aizu (as outlined in Tab. 2).[26] If the paraelectric phases belong to the centrosymmetric point groups, the ferroelectrics are reversible, in which the direction of the P_s can be reversed under the external electric field. Whereas on condition that the paraelectric phases crystallize in the polar point groups, the ferroelectrics are reorientable, in which the direction of the

P_s can just be reoriented instead of be reversed. The reversible ferroelectrics are more common than those reorientable ones. In any case, when the point group symmetry of one phase is known, that of another phase and the direction of the P_s can be inferred from Tab. 2, under the guidance of the Curie symmetry principle.

Tab. 1 68 ferroelectric space groups belonging to the 10 polar point groups

Point group	**Space group**
C_1	*P*1
C_2	*P*2, *P*2$_1$, *C*2
C_{1h}	*Pm, Pc, Cm, Cc*
C_{2v}	*Pmm*2, *Pmc*2$_1$, *Pcc*2, *Pma*2, *Pca*2$_1$, *Pnc*2, *Pmn*2$_1$, *Pba*2, *Pna*2$_1$, *Pnn*2, *Cmm*2, *Cmc*2$_1$, *Ccc*2, *Amm*2, *Abm*2, *Ama*2, *Aba*2, *Fmm*2, *Fdd*2, *Imm*2, *Iba*2, *Ima*2
C_4	*P*4, *P*4$_1$, *P*4$_2$, *P*4$_3$, *I*4, *I*4$_1$
C_{4v}	*P*4*mm*, *P*4*bm*, *P*4$_2$*cm*, *P*4$_2$*nm*, *P*4*cc*, *P*4*nc*, *P*4$_2$*mc*, *P*4$_2$*bc*, *I*4*mm*, *I*4*cm*, *I*4$_1$*md*, *I*4$_1$*cd*
C_3	*P*3, *P*3$_1$, *P*3$_2$, *R*3
C_{3v}	*P*3*m*1, *P*31*m*, *P*3*c*1, *P*31*c*, *R*3*m*, *R*3*c*
C_6	*P*6, *P*6$_1$, *P*6$_5$, *P*6$_2$, *P*6$_4$, *P*6$_3$
C_{6v}	*P*6*mm*, *P*6*cc*, *P*6$_3$*cm*, *P*6$_3$*mc*

Tab. 2 88 species of potential paraelectric-to-ferroelectric phase transitions

Triclinic	$\bar{1}$*F*1 (1)
Monoclinic	2*F*1 (2/2); *mF*1 (2/2); 2/*mF*1 (2); 2/*mFm* (1); 2/*mF2* (1)
Orthorhombic	222*F*1 (4/2); 222*F*2 (1); *mm*2*F*1 (4/2); *mm*2*Fm* (2/2); *mmmF*1 (4); *mmmFm* (2); *mmmFmm*2 (1)
Tetragonal	4*F*1 (4/2); $\bar{4}$*F*1 (4/2); $\bar{4}$*F*2 (1); 4/*mF*1 (4); 4/*mFm* (2); 4/*mF*4 (1); 422*F*1 (8/2); 422*F*2(*s*) (2); 422*F*4 (1); 4*mmF*1 (8/2); 4*mmFm* (4/2); $\bar{4}$2*mF*1 (8/2); $\bar{4}$2*mF*2(*s*) (2); $\bar{4}$2*mFm* (4/2); $\bar{4}$2*mFmm*2 (1); 4/*mmmF*1 (8); 4/*mmmFm*(*s*) (4); 4/*mmmFm*(*p*) (4); 4/*mmmFmm*2(*s*) (2); 4/*mmmF*4*mm* (1)
Trigonal	3*F*1 (3/2); $\bar{3}$*F*1 (3); $\bar{3}$*F*3 (1); 32*F*1 (6/2); 32*F*2 (3/2); 32*F*3 (1); 3*mF*1 (6/2); 3*mFm* (3/2); $\bar{3}$*mF*1 (6); $\bar{3}$*mF*2 (3); $\bar{3}$*mFm* (3); $\bar{3}$*mF*3*m* (1)
Hexagonal	6*F*1 (6/2); $\bar{6}$*F*1 (6/2); $\bar{6}$*Fm* (3/2); $\bar{6}$*F*3 (1); 6/*mF*1 (6); 6/*mFm* (3); 6/*mF*6 (1); 622*F*1 (12/2); 622*F*2(*s*) (3); 622*F*6 (1); 6*mmF*1 (12/2); 6*mmFm* (6/2); $\bar{6}$*m*2*F*1 (12/2); $\bar{6}$*m*2*Fm*(*s*) (6/2); $\bar{6}$*m*2*Fm*(*p*) (6/2); $\bar{6}$*m*2*Fmm*2 (3/2); $\bar{6}$*m*2*F*3*m* (1); 6/*mmmF*1 (12); 6/*mmmFm*(*s*) (6); 6/*mmmFm*(*p*) (6); 6/*mmmFmm*2(*s*) (3); 6/*mmmF*6*mm* (1)
Cubic	23*F*1 (12/2); 23*F*2 (3); 23*F*3 (4/2); *m*$\bar{3}$*F*1 (12); *m*$\bar{3}$*Fm* (6); *m*$\bar{3}$*Fmm*2 (3); $\bar{3}$*F*3 (4); 432*F*1 (24/2); 432*F*2(*s*) (6); 432*F*4 (3); 432*F*3 (4); $\bar{4}$3*mF*1 (24/2); $\bar{4}$3*mFm* (12/2); $\bar{4}$3*mFmm*2 (3); $\bar{4}$3*mF*3*m* (4/2); *m*$\bar{3}$*mF*1 (24); *m*$\bar{3}$*mFm*(*s*) (12); *m*$\bar{3}$*mFm*(*p*) (12); *m*$\bar{3}$*mFmm*2 (6); *m*$\bar{3}$*mF*4*mm* (3); *m*$\bar{3}$*mF*3*m* (4)

* *F* indicates the paraelectric-to-ferroelectric phase transition, while *p* and *s* mean that symmetry elements of the ferroelectric phase correspond to the principal and side symmetric axes in the paraelectric phase, respectively. State numbers are included in the round brackets, while the simple numbers represent reversible ferroelectrics. The number of 1 belongs to 18 types of uniaxial ferroelectrics, and the numbers greater than 1 are the sums of equivalent polar directions of multiaxial ferroelectrics. Besides, for the complex state numbers like "3/2", "4/2" and so on, the common number of 2 on the right of the forward slash indicates reorientable ferroelectrics, whereas the numbers on the left of it denote the sums of equivalent polar directions.

However, the differences between crystal structures in the paraelectric and ferroelectric phases are so small that the verifications of the point group symmetries are always difficult. In many instances, some symmetry elements like inversion center in the paraelectric phase will "survive" in the ferroelectric one, taking the form of pseudo-symmetry. Even though a variety of diffraction methods have been extensively applied, it seems hard to identify the pseudo-symmetry by the single-crystal X-ray diffraction or the neutron diffraction. Fortunately, inspired by the Neumann's principle, second harmonic generation (SHG) technique has been developed as an indispensable supplementary approach.[27–31] SHG is a second-order nonlinear optical phenomenon involving the doubling of the incident light frequency and is described by the second-order nonlinear coefficient ($\chi^{(2)}$). As a third rank polar tensor, $\chi^{(2)}$ vanishes in the 11 centrosymmetric point groups and the 3 noncentrosymmetric-nonpolar point groups 422 (D_4), 622 (D_6) and 432 (O).[32] It means that the crystals belonging to the above 14 point groups are not able to display SHG effect, and accordingly, only the other 18 point groups including the 10 polar point groups are SHG-active. This makes the SHG technique very important and useful in detecting the lack of inversion symmetry and the emergence of ferroelectricity.[31] In particular, the change of the temperature-dependent SHG signal from an inactive state to an active state indicates a centrosymmetric-to-noncentrosymmetric phase transition, being a strong evidence of the reversible

ferroelectrics. As for the noncentrosymmetric-to-polar phase transition, both phases are SHG-active, but the variation of SHG intensity will be apparent. What is more, the dependence of $\chi^{(2)}$ as a function of temperature matches well with that of P_s, in accordance with the Landau expression $\chi^{(2)} = 6\varepsilon_0\beta P_s$, where ε_0 is the vacuum dielectric constant and β is nearly independent of the temperature.[33]

Notably, it should be realized that ferroelectrics can't be distinguished solely by the symmetry considerations, but also by the experimental characteristics like critical phenomena, ferroelectric hysteresis loop and electric domains. Critical phenomena, as the name suggests, mean that the dielectric, piezoelectric, pyroelectric properties and the above-mentioned SHG effects of ferroelectrics will display significant anomalies in the vicinities of the critical temperatures. In particular, the temperature-dependent dielectric constant will be more than double near T_c, suggesting a notable change in the polarity of crystal structure and being a direct sign of the paraelectric-to-ferroelectric phase transition. Considering the typically polarization switching, ferroelectric hysteresis loop is indeed the most important character of ferroelectrics. In the paraelectric phase, there is a linear relationship between the polarization (P) and the electric field (E), while the nonlinear P–E curve emerging in the ferroelectric phase is known as ferroelectric hysteresis loop (Fig. 1).

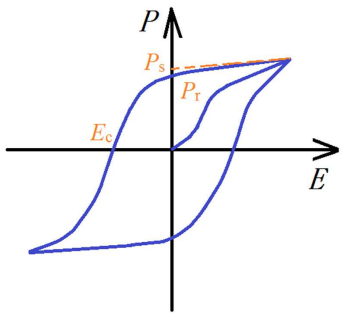

Fig. 1 A typical ferroelectric hysteresis loop shows the spontaneous polarization (P_s), the remnant polarization (P_r) and the coercive field (E_c).

Herein, the major emphasis of this review is on how to obtain high-performance molecular ferroelectrics on the basis of the connection between the symmetry breaking and the ferroelectricity. For a crystal, once a phase adopting one of the 68 polar space groups (Tab. 1) is supposed to be ferroelectric, the paraelectric phase should exist in the high-temperature region. Meanwhile, in the case of an assumed paraelectric phase, the corresponding ferroelectric phase ought to be found in the low-temperature region. It is the Curie symmetry principle that determines the group-subgroup relationship between the two phases (Tab. 2). In the light of the Neumann's principle, the temperature-dependent SHG signal and dielectric constant are particularly sensitive to the symmetry breaking from the paraelectric point group to the ferroelectric one. Furthermore, ferroelectric hysteresis loop and electric domains can give more evidence of ferroelectricity. Based on these, we present our systematic works concerning molecular ferroelectrics.

2 Order−disorder and displacive types of ferroelectrics

Generally speaking, the mechanisms of ferroelectrics fall into two major categories: (1) order−disorder type, for which the reorientation of ions from a disordered state to an ordered state leads to the ferroelectricity;[34,35] (2) displacive type, for which the ferroelectricity arises from the relative displacement of ions.[36] It must be pointed out that, in actual situations, quite a few ferroelectrics seem to combine the characteristics of both order−disorder and displacive types. For example, in the case of the typical hydrogen-bonded ferroelectric KH_2PO_4, the ferroelectricity is triggered by the ordering of protons but mainly comes from the displacement of K^+ and PO_4^{3-} ions along the polar axis.[37]

2.1 $[(Me_2CH)_2NH_2]X$ (X = Cl^- (1) and Br^- (2))

A series of simple organic salts [(HDABCO)X] (DABCO = 1,4-diazabicyclo[2.2.2]

octane, X = ClO_4^-, BF_4^-, ReO_4^-) has been reported as KH_2PO_4-type molecular ferroelectrics with high T_c in the range of 374−378 K.[38,39] Enlightened by this, based on some amines like dimethylamine, trimethylamine, diisopropylamine and aniline derivatives which can easily undergo order−disorder transitions, the simple organic salts with polar point groups at room temperature are great candidates for high-temperature ferroelectrics suitable for practical applications. That is why diisopropylammonium chloride and bromide were noticed during searching the Cambridge Structure Database, since the space groups of them were recorded as one of the 68 ferroelectric space groups (Tab.1) at room temperature, *i.e.* $P2_1$ (polar point group 2 (C_2)) (the respective reference codes are JAYPUU01 for $[(Me_2CH)_2NH_2]Cl$ (**1**) and TEJKUO for $[(Me_2CH)_2NH_2]Br$ (**2**)). These two compounds turn out to display excellent ferroelectric properties comparable to those of $BaTiO_3$ and poly(vinylidene difluoride) (PVDF).[40,41]

According to the Curie symmetry principle, the possible paraelectric phases should appear above room temperature and have higher symmetries. To detect symmetry breaking as well as phase transitions, the temperature-dependent ε' (the real part of the complex dielectric constant) along the *b* axis at 1 kHz and the temperature-dependent SHG responses were measured for compounds **1** and **2** in the high-temperature zone (Fig. 2, 3). The noticeable anomalies of ε' observed at 440 K for **1** (from about 50 to 450) and at 426 K for **2** (from about 140 to 1300) are typical for ferroelectric phase transitions, and the two Curie temperatures are much higher than many known molecular ferroelectrics. In both cases, the SHG signal exhibits an abrupt rise from zero above T_c to a saturation value below T_c, revealing the symmetry breaking from a centrosymmetric paraelectric phase to a noncentrosymmetric ferroelectric phase.

Undoubtedly, the crystal structures of compounds **1** and **2** characterized in the

paraelectric phases belong to the centrosymmetric space group $P2_1/m$ (nonpolar point group $2/m$ (C_{2h})). The ferroelectric space group $P2_1$ is a subgroup of the paraelectric $P2_1/m$ whose maximal non-isomorphic subgroups include Pm, $P2_1$ and $P\bar{1}$, obeying the Curie symmetry principle. As depicted in Scheme 1a, symmetry breaking occurs with an Aizu notation of $2/mF2$, while the macroscopic symmetry elements decrease from four (E, C_2, i, σ_h) in the paraelectric point group $2/m$ (C_{2h}) to two (E, C_2) in the ferroelectric 2 (C_2). The loss of mirror plane (σ_h) and inversion center (i) are in good agreement with the decrease of microscopic symmetry operations reflected by the change of the space group (Scheme 1b).

The crystal structures and phase transition mechanisms of compounds **1** and **2** are almost identical. In the paraelectric phase, the N atom of the $[(Me_2CH)_2NH_2]^+$ cation is disordered over two sites and distributed equally over the mirror plane perpendicular to the b axis (Fig. 4a). Several C atoms of the $[(Me_2CH)_2NH_2]^+$ cation and the Cl^- anion are located at this mirror plane, too. As a result of decreasing temperature, the N atom becomes ordered, and the Cl^- anion deviates from the cation along the b-axis direction. Consequently, the mirror plane and inversion center are missing, and a polar crystal structure appears in the ferroelectric phase (Fig. 4b). The order−disorder transition of N atom triggers the symmetry breaking, whereas the atomic displacement governs the ferroelectricity developing along the b axis.

For **1**, at 10 Hz, a fine ferroelectric hysteresis loop is obtained just below T_c = 440 K. The P_s of about 8.9 μC cm^{-2} is close to that of PVDF (8.0 μC cm^{-2}) (Fig. 2b). By the substitution of Cl^- ion by Br^- ion, a slightly lower T_c of 426 K and a comparable P_s were observed for **2**. Below T_c, the ferroelectric hysteresis loop measured at 25 Hz bears a close resemblance to the case of **1** (Fig. 3b). More notably, **2** is prominent in pyroelectric effect, for which the extraordinary high P_s of 23 μC cm^{-2} can be

compared with that of $BaTiO_3$ (26 μC cm^{-2}) (Fig. 3a). The similar trends of P_s and $\chi^{(2)}$ triggered by temperature verify the transition from the paraelectric phase to the ferroelectric one.

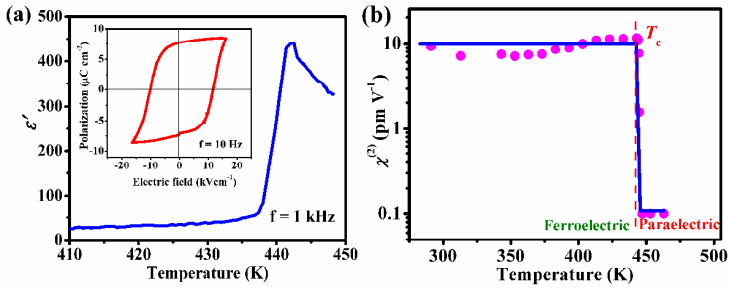

Fig. 2 (a) Temperature-dependent ε' along the *b* axis of **1**. Inset: ferroelectric hysteresis loop recorded at 418 K. (b) Temperature-dependent $\chi^{(2)}$.

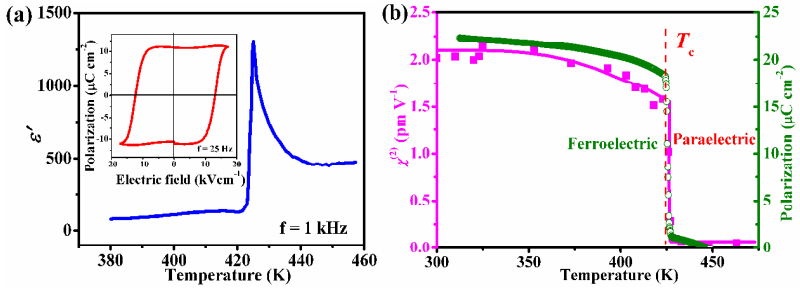

Fig. 3 (a) Temperature-dependent ε' along the *b* axis of **2**. Inset: ferroelectric hysteresis loop measured at 416 K. (b) $\chi^{(2)}$ and spontaneous polarization *versus* temperature.

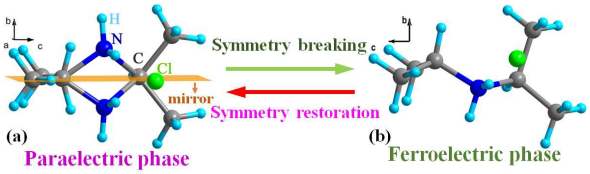

Fig. 4 Molecular structures of **1**: symmetry breaking from (a) the high-temperature paraelectric phase to (b) the low-temperature ferroelectric phase.

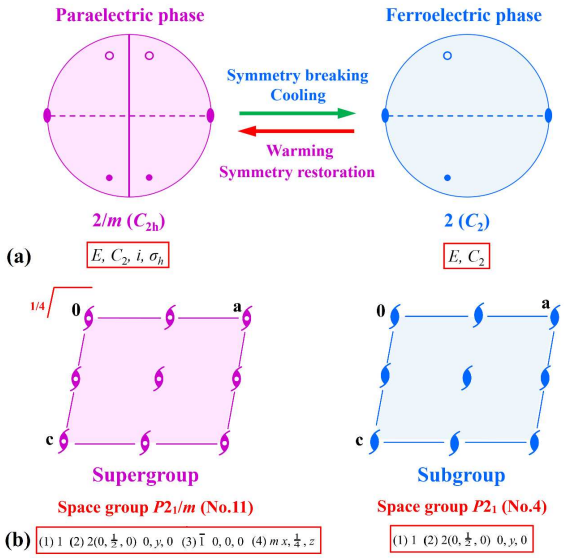

Scheme 1 Symmetry breaking occurs with an Aizu notation of 2/*mF*2 in compounds **1** and **2**. (a) Equatorial plane projection of point groups 2/*m* (C_{2h}) in the paraelectric phase and 2 (C_2) in the ferroelectric phase. (b) Spatial symmetry operations of the space groups $P2_1/m$ in the paraelectric phase and $P2_1$ in the ferroelectric phase.

2.2 [4-NCCH$_2$-PhNH$_3$]ClO$_4$ (3)

Using the principle analogous to the above cases, a new simple organic salt, 4-(cyanomethyl)anilinium perchlorate ([4-NCCH$_2$-PhNH$_3$]ClO$_4$ (**3**)), was synthesized.[42] However, introducing aromatic cation and tetrahedral anion with large size makes compound **3** a low-temperature displacive-type ferroelectric. At room temperature, it crystallizes in a centrosymmetric space group $P2_1/m$ with the ordered [4-NCCH$_2$-PhNH$_3$]$^+$ cation and the seriously disordered ClO_4^- anion located at the mirror plane perpendicular to the *b* axis, probably corresponding to a paraelectric phase (Fig. 5a). A drop in temperature may easily turn the disordered ClO_4^- anion into an ordered state and thus evoke dipole moment or ferroelectricity in the crystal lattice. To detect whether it is true, the measurement of temperature-dependent ε' along the *b* axis was performed in the cooling process at 1 kHz. The fact that the ε' increases by two orders

of magnitude at around T_c = 184 K strongly supports a paraelectric-to-ferroelectric phase transition (Fig. 6a).

Accompanying the phase transition, the temperature-dependent SHG signal varies between zero and a saturation value, indicating the inversion symmetry breaking from a centrosymmetric paraelectric phase to a noncentrosymmetric ferroelectric phase (Fig. 6a). Furthermore, the curve of P_s *versus* temperature deduced from the pyroelectric measurement is consistent with that of $\chi^{(2)}$, disclosing the paraelectric behavior above T_c and the ferroelectric behavior below T_c (Fig. 6a). Given that, below T_c, the crystal structure of the ferroelectric phase is determined as a polar space group $P2_1$ (Fig. 5b). The ClO_4^- anion is ordered and manifests apparent displacement together with the cation, originating the symmetry breaking process from $P2_1/m$ to $P2_1$. It is similar to the above-mentioned cases of compounds **1** and **2**.

As illustrated in Fig. 6b, the linear P–E relationship above T_c is an indicator of paraelectric phase. By contrast, at 100 Hz, the standard ferroelectric hysteresis loop only appears below T_c. The P_s is measured as 0.75 μC cm^{-2} comparable to the theoretical value calculated by the shift of the centers of positive and negative ions. It indicates that the ferroelectricity arises principally from the atomic displacements instead of the order–disorder behavior of the ClO_4^- anion.

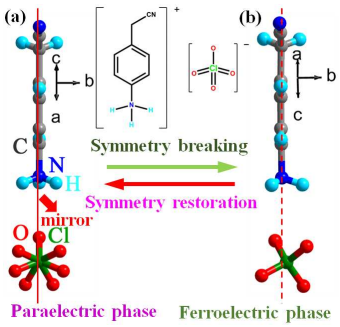

Fig. 5 Molecular structures of **3**: symmetry breaking from (a) the high-temperature paraelectric phase to (b) the low-temperature ferroelectric phase.

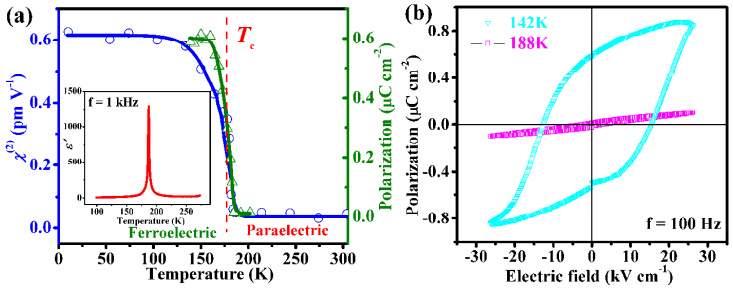

Fig. 6 (a) Temperature dependence of $\chi^{(2)}$ and spontaneous polarization of **3**. Inset: temperature-dependent ε' along the *b* axis. (b) Ferroelectric hysteresis loops measured at 142 and 188 K.

2.3 [DABCOO$_2$][*L*-C$_4$H$_4$O$_6$] (4)

Among the 10 polar point groups there are 5 chiral ones, *i.e.* 1 (C_1), 2 (C_2), 4 (C_4), 3 (C_3) and 6 (C_6), from which 20 chiral-ferroelectric space groups can be derived (Tab.1). As depicted in Tab.2, therefore, up to 22 species of paraelectric-to-ferroelectric phase transitions are found to be chiral-to-chiral. Due to the chirality and hydrogen donor/acceptor functionalities, *L*-tartaric acid always guides the crystallization of hydrogen-bonded complexes in the chiral and even polar point groups. Diverse transformations of hydrogen bonds make this family of complexes available in constructing potential ferroelectrics. For example, the famous ferroelectric, Rochelle salt, undergoes a symmetry-breaking phase transition from a chiral space group $P2_12_12$ (nonpolar point group 222 (D_2)) to a chiral $P2_1$ (polar point group 2 (C_2)), resulting from the proton dynamics of the hydroxyl group of *L*-tartrate.[18] Thus the supramolecular adduct of 1,4-diazabicyclo [2.2.2]octane N,N′-dioxide and *L*-tartaric acid, abbreviated as [DABCOO$_2$][*L*-C$_4$H$_4$O$_6$] (**4**), was designed for its potential ferroelectricity.[43]

In the room-temperature phase, **4** crystallizes in a chiral space group $P4_12_12$ (nonpolar point group 422 (D_4)), corresponding to a paraelectric phase. The twofold rotation axes along the [1 1 0] and [1 −1 0] directions are occupied by the disordered

[$DABCOO_2$] molecules and the ordered [*L*-$C_4H_4O_6$] molecules (Fig. 7a). As shown in Tab.2, the ferroelectric phase should appear below room temperature and belong to one of the three chiral-polar point groups 1 (C_1), 2 (C_2), 4 (C_4). The temperature dependence of ε' along the *c* axis gives a prominent anomaly with a peak value of about 800 at 1 kHz at around 254 K (Fig. 8a). Then coupled with the temperature-dependent polarization (Fig. 8a), a paraelectric-to-ferroelectric phase transition at T_c = 254 K is suggested.

For the crystal structure characterized in the ferroelectric phase below T_c, the hydrogen bonds have geometries which are nearly identical to those in the paraelectric phase. However, the [$DABCOO_2$] molecules go from disordered to ordered (Fig. 7b). Markedly, along the *c*-axis direction, there is a relative displacement of 0.1344 Å between the [$DABCOO_2$] and [*L*-$C_4H_4O_6$] components. Therefore, the symmetry elements of twofold rotation axes (C'_2, C''_2) disappear in the [1 1 0], [1 −1 0] and *b*-axis directions, generating a chiral space group $P4_1$ (polar point group 4 (C_4)) in the ferroelectric phase. As shown in Scheme 2, the symmetry breaking is accompanied by the decrease of symmetry elements from eight (E, $2C_4$, C_2, $2C'_2$, $2C''_2$) in the paraelectric point group 422 (D_4) to four (E, $2C_4$, C_2) in the ferroelectric point group 4 (C_4). This chiral-to-chiral phase transition abides by the Curie symmetry principle, seeing that $P4_1$ is a subgroup of $P4_12_12$ whose maximal non-isomorphic subgroups contain $P4_1$, $C222_1$ and $P2_12_12_1$.

For this uniaxial ferroelectric with an Aizu notation of 422*F*4, the ferroelectricity along the *c* axis arises from the reorientation of O–H bonds caused by the relative displacement between the two molecular sublattices. Consequently, the ferroelectric mechanism of **4** is regarded as displacive type, differing from the familiar proton transfers in the general hydrogen-bonded ferroelectrics. The negligible deuteration

effect also supports this argument. At 50 Hz, the nice ferroelectric hysteresis loop is measurable only below T_c, directly demonstrating the ferroelectricity (Fig. 8b). And, the P_s is comparable to those of the Rochelle salt and its analogue compounds (0.25−1 μC cm^{-2}).

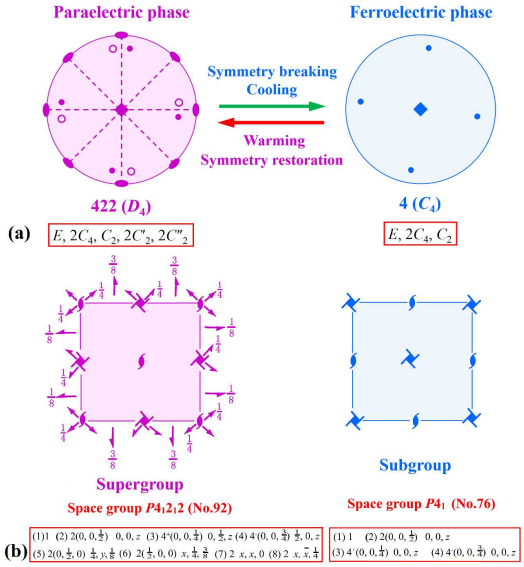

Scheme 2 Symmetry breaking occurs with an Aizu notation of 422*F*4 in **4**. (a) Equatorial plane projection of point groups 422 (D_4) in the paraelectric phase and 4 (C_4) in the ferroelectric phase. (b) Spatial symmetry operations of the space groups $P4_12_12$ in the paraelectric phase and $P4_1$ in the ferroelectric phase.

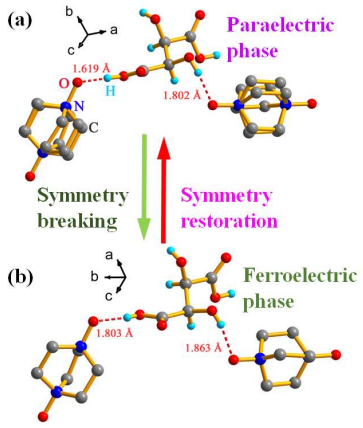

Fig. 7 Molecular structures of **4**: symmetry breaking from (a) the high-temperature paraelectric phase to (b) the low-temperature ferroelectric phase. The red dotted lines

signify the hydrogen bonds.

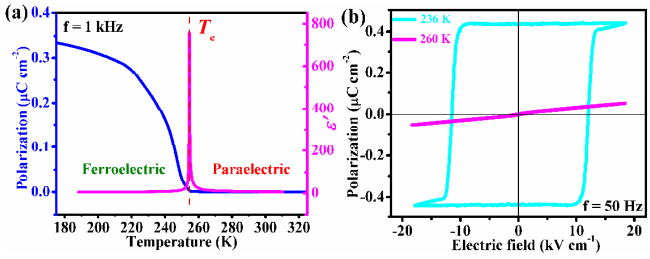

Fig. 8 (a) Temperature dependence of spontaneous polarization and ε' along the *c* axis of **4**. (b) Ferroelectric hysteresis loops measured at 236 and 260 K.

2.4 $Ca(NO_3)_2$(15-crown-5) (5)

A new displacive-type metal−organic ferroelectric, (15-crown-5)bis(nitrato-O,O′)-calcium (II) (*i.e.* $Ca(NO_3)_2$(15-crown-5) (**5**)), is a great example of how to seek for the low-temperature molecular ferroelectrics from the Cambridge Structure Database.[44] Therein two polymorphs of **5** were recorded, that is, a centrosymmetric *Pbca* (nonpolar point group *mmm* (D_{2h})) at room temperature and a noncentrosymmetric $Pca2_1$ (polar point group *mm*2 (C_{2v})) at low temperature (the respective reference codes are JAWQUT and JAWQUT01). The maximal non-isomorphic subgroups of *Pbca* include $Pca2_1$, $P2_12_12_1$ and $P2_1/c$, abiding by the Curie symmetry principle. The symmetry elements decrease from eight (E, C_2, $2C'_2$, i, σ_h, $2\sigma_v$) in the room-temperature point group *mmm* (D_{2h}) to four (E, C_2, $2\sigma_v$) in the low-temperature *mm*2 (C_{2v}), and the spatial symmetry change is depicted in Scheme 3. Symmetry breaking occurs, along with the disappearance of the symmetry elements of inversion center (i), mirror plane (σ_h) and twofold rotation axis (C'_2). Crystal structures in the two phases are compared with each other (Fig. 10). The Ca^{2+} ion is nine-coordinated by five O atoms from the crown ether and four O atoms from the two planar NO_3^- anions, and the dihedral angle between the NO_3^- planes shows a marked variation from 75.32° in the room-temperature phase to 63.2° and 87.99° in the low-temperature phase.

Evidently, the coordination environment of the Ca^{2+} ion is distorted, thereby inducing the symmetry-breaking phase transition. Because such kind of coordination distortion has been proved to induce ferroelectricity in compounds like $BaTiO_3$,[45,46] Compound **5** is reasonably expected to undergo a paraelectric-to-ferroelectric phase transition with an Aizu notation of *mmmFmm*2.

The temperature dependence of ε' along the *c* axis demonstrates a notable anomaly with a peak value of about 350 approaching T_c = 205 K at 1 kHz, revealing the occurrence of a low-temperature ferroelectric phase transition (Fig. 9a). Moreover, in view of the temperature-dependent SHG signal which is similar to the temperature dependence of P_s, the gradual change of $\chi^{(2)}$ from the SHG-inactive state above T_c to the SHG-active state below T_c verifies the inversion symmetry breaking (Fig. 9a). The linear-to-nonlinear variation of the *P*–*E* relationship matches well with the paraelectric-to-ferroelectric phase transition (Fig. 9b). According to the saturated ferroelectric hysteresis loop at 50 Hz, the P_s along the *c* axis reaches about 0.5 μC cm^{-2}.

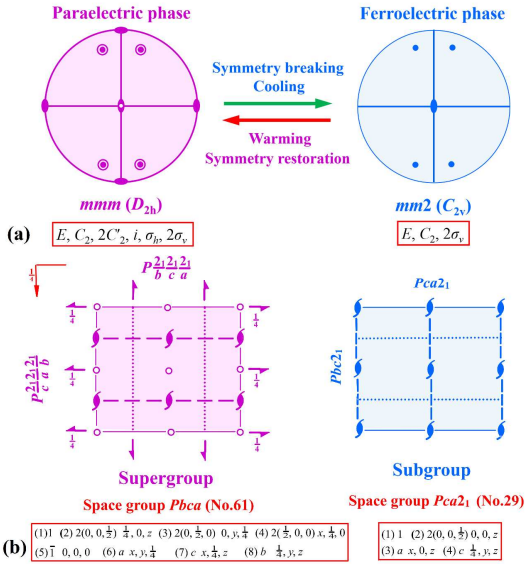

Scheme 3 Symmetry breaking occurs with an Aizu notation of *mmmFmm*2 in **5**. (a) Equatorial plane projection of point groups *mmm* (D_{2h}) in the paraelectric phase and

*mm*2 (C_{2v}) in the ferroelectric phase. (b) Spatial symmetry operations of the space groups *Pbca* in the paraelectric phase and $Pca2_1$ in the ferroelectric phase.

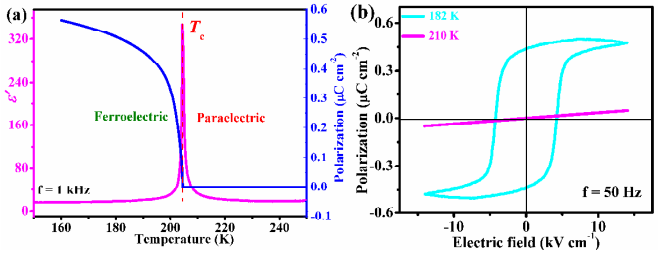

Fig. 9 (a) Temperature dependence of spontaneous polarization and ε' along the *c* axis of **5**. (b) Ferroelectric hysteresis loops measured at 182 and 210 K.

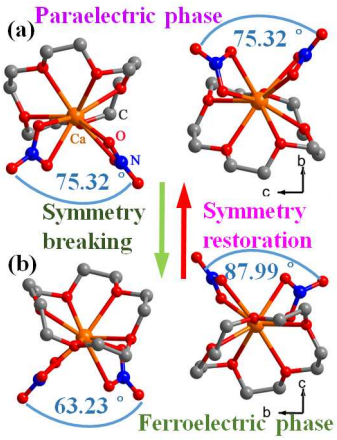

Fig. 10 Crystal structures of **5**: symmetry breaking from (a) the high-temperature paraelectric phase to (b) the low-temperature ferroelectric phase. The blue curves represent the dihedral angles between the NO_3^- planes.

3 Rotator-stator-type molecular ferroelectrics

Molecular machines like molecular propellers, gears, ratchets, turnstiles, gyroscopes and compasses in which the molecular motions or dynamics could be controlled by the external stimuli, are able to incorporate multiple properties into a single system and have great potential in the development of functional materials.[47] Given that, a type of supramolecular rotator systems consisting of crown ethers and organic cations deserve attention. The cooperation effect between the two components

will cause various architectures and molecular dynamics. As molecular self-assemblies constructed through supramolecular interactions like hydrogen bonds, such kind of supramolecular adducts are allowed to make molecular motions or dynamics controllable by an external electric field, giving rise to rotator-stator-type molecular ferroelectrics easily. For example, the ferroelectric behavior of the hydrogen-bonding assembly, (*m*-fluoroanilinium)(dibenzo[18]crown-6)[Ni(dmit)$_2$], (dmit^{-2} = 2-thioxo-1,3-dithiole-4,5-dithiolate), is attributed to the dipolar rotation of *m*-fluoroanilinium.[48]

3.1 [(4-CH_3O-$PhNH_3$)(18-crown-6)]A (A = ReO_4^- (6) and BF_4^- (7))

As a polarization rotation unit similar to *m*-fluoroanilinium, 4-methoxyanilinium is selected to build a hydrogen-bonding assembly with flexible 18-crown-6 and perrhenate. The 4-methoxyanilinium cation is anchored in the cavity of the 18-crown-6 molecule by N–H···O hydrogen-bonding interactions.[49] In the room-temperature phase, [(4-CH_3O-$PhNH_3$)(18-crown-6)]ReO_4 (**6**) crystallizes in a centrosymmetric space group *Pnma* (nonpolar point group *mmm* (D_{2h})) having eight symmetry elements (E, C_2, $2C'_2$, i, σ_h, $2\sigma_v$). The disordered [4-CH_3O-$PhNH_3$]$^+$ cation which is acting as a rotator, the 18-crown-6 molecule which is treated as the stator and the BF_4^- anion lie on a mirror plane perpendicular to the *b* axis together, looking like an ancient Chinese bola (Fig. 11a). If the temperature decreases, the [4-CH_3O-$PhNH_3$]$^+$ cation is expected to get ordered and thus generate a lower-symmetry ferroelectric phase below room temperature.

Along the *c* axis, ε' as a function of temperature is notably anomalous with a high peak value of about 730 at 1 MHz approaching T_c = 153 K, in line with a paraelectric-to-ferroelectric phase transition (Fig. 12). At around T_c, the rapid increase of SHG signal from a zero value above T_c to a saturation value below T_c is corresponded to a

centrosymmetric-to-noncentrosymmetric phase transition (Fig. 12). Not surprisingly, when the temperature decreases down to below T_c, the mirror symmetry perpendicular to the *b* axis (σ_h) is broken as the $[4\text{-}CH_3O\text{-}PhNH_3]^+$ cation gets ordered (Fig. 11b). The symmetry elements of inversion center (*i*) and the two-fold screw axes (C'_2) along the *a*-, *c*-axis directions are also lost, while the two-fold screw axis along the *b* axis is still preserved. Accordingly, in the low-temperature phase, **6** adopts a noncentrosymmetric space group $Pna2_1$ (polar point group $mm2$ (C_{2v})) having four symmetry elements (E, C_2, $2\sigma_v$). The symmetry breaking process is described by an Aizu notation of *mmmFmm*2, with the decrease of symmetry elements from eight to four (Scheme 4). Besides, $Pna2_1$ is a subgroup of *Pnma* which has maximal non-isomorphic subgroups as $Pna2_1$, $Pmn2_1$, $Pmc2_1$, $P2_12_12_1$, $P2_1/c$ and $P2_1/m$, obeying the Curie symmetry principle.

As for the curves of polarization *versus* electric field recorded at different temperatures, the linear one above T_c suggests the paraelectric phase, whereas the nonlinear one manifests the ferroelectric behavior, consistent with the symmetry breaking (Fig. 12). The P_s along the *c* axis is about 1.2 μC cm^{-2} at 50 Hz, which is much higher than that of the Rochelle salt. The ferroelectricity accompanying the symmetry-breaking phase transition is aroused by the pendulum motion of the $[4\text{-}CH_3O\text{-}PhNH_3]^+$ rotator.

Also, the supramolecular adducts containing other tetrahedral anions as $[BF_4]^-$ and $[ClO_4]^-$ should have similar ferroelectric phase transitions with the perrhenate analogue. It has been proved that $[(4\text{-}CH_3O\text{-}PhNH_3)(18\text{-crown-}6)]BF_4$ (**7**) also undergoes a symmetry-breaking phase transition from *Pnma* to $Pna2_1$.[50] As a consequence of the replacement of ReO_4^- anion by BF_4^-anion, however, the T_c decreases to 127 K, and the P_s along the *c* axis is obtained as about 0.54 μC cm^{-2} from

the perfect ferroelectric hysteresis loop at 50 Hz.

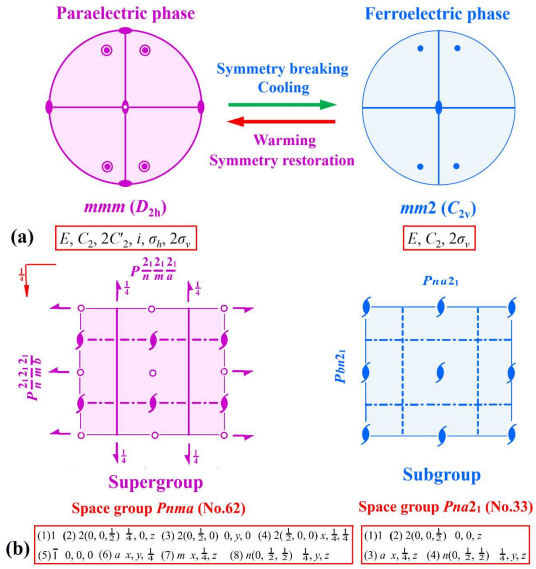

Scheme 4 Symmetry breaking occurs with an Aizu notation of *mmmFmm*2 in compounds **6** and **7**. (a) Equatorial plane projection of point groups *mmm* (D_{2h}) in the paraelectric phase and *mm*2 (C_{2v}) in the ferroelectric phase. (b) Spatial symmetry operations of the space groups *Pnma* in the paraelectric phase and $Pna2_1$ in the ferroelectric phase.

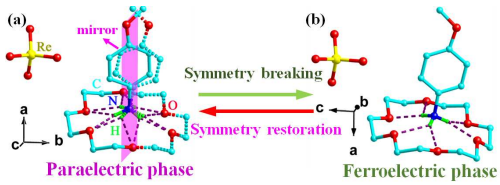

Fig. 11 Molecular structures of **6**: symmetry breaking from (a) the high-temperature paraelectric phase to (b) the low-temperature ferroelectric phase.

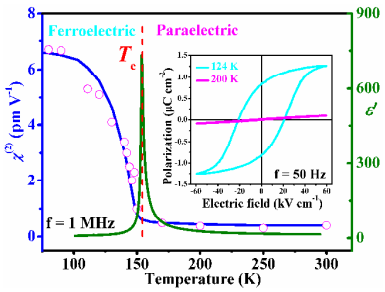

Fig. 12 Temperature dependence of $\chi^{(2)}$ and ε' along the *c* axis of **6**. Inset: ferroelectric

hysteresis loops measured at 124 and 200 K.

3.2 [(DIPA)(18-crown-6)]A (DIPA = 2,6-diisopropylanilinium, A = BF_4^- (8) and ClO_4^- (9))

In order to achieve ferroelectricity different from that observed in the above-mentioned compounds **6** and **7**, the polar $(4\text{-}CH_3O\text{-}PhNH_3)^+$ cation experiencing pendulum motion is replaced by the 2,6-diisopropylanilinium cation which possesses a intramolecular mirror plane and two bulky isopropyl groups. Molecular motion may be hampered with temperature decrease, resulting in the formation of dipole moment. Then [(DIPA)(18-crown-6)]BF_4 (**8**) and [(DIPA)(18-crown-6)]ClO_4 (**9**) were obtained as two new host-guest-type ferroelectrics.[51,52] N–H···O hydrogen-bonding interactions hold the $[DIPA]^+$ cation in the cavity of 18-crown-6 molecule to form a supramolecular assembly, in which the $[DIPA]^+$ cation acts as a stator but the 18-crown-6 molecule acts like a rotator.

For **8**, the crystal structure at room temperature belongs to a centrosymmetric space group *Pbcn* (nonpolar point group *mmm* (D_{2h})), which possesses eight symmetry elements (E, C_2, $2C'_2$, i, σ_h, $2\sigma_v$). The 18-crown-6 molecules and the $[DIPA]^+$ cations are ordered, whereas partial BF_4^- anions are disordered over two orientations (Fig. 13a). Apparently, this nonpolar phase should only be regarded as a paraelectric phase, and based on the Curie symmetry principle, the ferroelectric phase will appear below room temperature. That is exactly what happened. Although there is a near-room-temperature phase transition that occurs at T_1 = 305 K, the crystal structure above T_1 resides in the nonpolar point group *mmm* (D_{2h}) with a centrosymmetric space group *Ibam*, while 18-crown-6 molecules and BF_4^- anions become disordered. The same symmetry elements in *Ibam* and *Pbcn* indicate the absence of symmetry breaking at T_1. It is in good agreement with the result of temperature-dependent SHG

measurement as given in Fig. 14a. In view of the small anomaly of the temperature-dependent ε' (Fig. 14b), we can exclude the possibility of ferroelectric phase transition above room temperature.

By contrast, as the temperature decreases, the ε' along the *c* axis at 1 MHz shows a great anomaly at T_2 = 120 K, corresponding to a paraelectric-to-ferroelectric phase transition (Fig. 14b). Below T_2, the measurable SHG response implies that the crystal structure turns into noncentrosymmetric. The temperature dependence of P_s calculated by integrating the pyroelectric current is similar to that of $\chi^{(2)}$ (Fig. 14b), due to the symmetry-breaking phase transition approaching T_2. Consequently, the crystal structure of **8** in the ferroelectric phase adopts a noncentrosymmetric space group $Pna2_1$ (polar point group $mm2$ (C_{2v})), which has four symmetry elements (E, C_2, $2\sigma_v$). Since $Pna2_1$ is a subgroup of *Pbcn* whose maximal non-isomorphic subgroups cover $Pna2_1$, *Pnc*2, $Pca2_1$, $P2_12_12$, $P2_1/c$ and $P2/c$, the Curie symmetry principle is fulfilled. Symmetry breaking occurs with an Aizu notation of *mmmFmm*2 (Scheme 5). The broken of symmetry elements like the twofold rotation axis (C'_2) along the *b*-axis direction and the inversion center (*i*) is attributed to the further ordering of the BF_4^- anions, that is, the BF_4^- anions in the ferroelectric phase appear to be well ordered.

Remarkably, the observation that the *P*−*E* curves at 50 Hz exhibit a linear feature above T_2 but possess a nearly rectangular shape below T_2 with a P_s value of about 0.3 μC cm^{-2}, is a strong proof that a paraelectric-to-ferroelectric phase transition occurs at T_2 (Fig 14b). Unlike the cases of compounds **6** and **7**, the origin of ferroelectricity of **8** is ascribed to the synergistic order−disorder transitions of 18-crown-6 molecule and BF_4^- anion rather than the motion of anilinium cation.

After the BF_4^- anion is substituted by the ClO_4^- anion, as expected, the resultant [(DIPA)(18-crown-6)]ClO_4 (**9**) and its analogue are isostructural. Likewise, it

undergoes a paraelectric-to-paraelectric phase transition from *Ibam* to *Pbcn* at 278 K and then a paraelectric-to-ferroelectric phase transition from *Pbcn* to $Pna2_1$ at 132 K. What is worth mentioning, during the characterization of the crystal structure in the ferroelectric phase, a pseudo center of symmetry is suggested. However, taking into account the SHG-active state below 132 K, the space group in the ferroelectric phase is conclusively noncentrosymmetric. Comparing with compound **8**, not only an identical symmetry-breaking phase transition but also a comparable ferroelectric property were found in compound **9**. Moreover, the P_s of about 0.35 μC cm^{-2} at 50 Hz is a little higher than that of compound **8**. Incidentally, Tang and co-workers reported two new potential high-temperature molecular ferroelectrics, cyclohexylammonium perchlorate 18-crown-6 and cyclohexylammonium tetrafluoroborate 18-crown-6 very recently, which are structurally analogous to compounds **6** and **8**.[53] Both of them crystallize in the polar space group $Pca2_1$ at room temperature and have phase transition temperatures above 390 K.

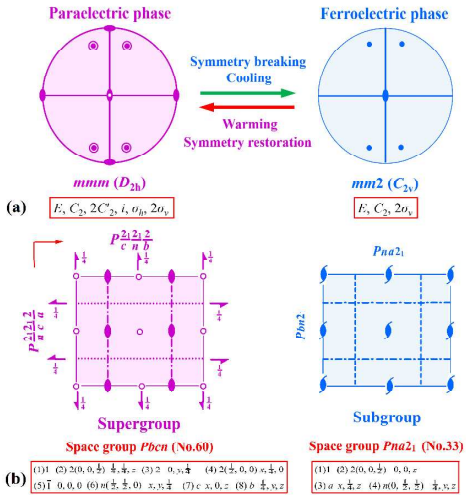

Scheme 5 Symmetry breaking occurs with an Aizu notation of *mmmFmm*2 in compounds **8** and **9**. (a) Equatorial plane projection of point groups *mmm* (D_{2h}) in the paraelectric phase and *mm*2 (C_{2v}) in the ferroelectric phase. (b) Spatial symmetry operations of the space groups *Pbcn* in the paraelectric phase and $Pna2_1$ in the

ferroelectric phase.

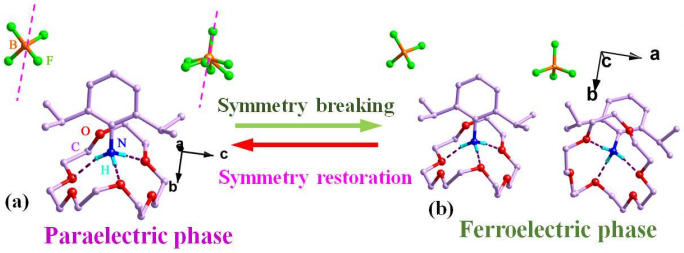

Fig. 13 Crystal structures of **8** in (a) the intermediate-temperature paraelectric phase and (b) the low-temperature ferroelectric phase. The dotted lines mean twofold rotation axes along the *b*-axis direction.

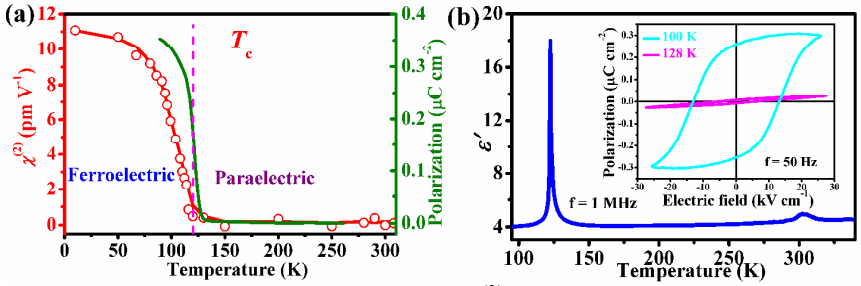

Fig. 14 (a) Temperature dependence of $\chi^{(2)}$ and spontaneous polarization of **8**. (b) Temperature-dependent ε' along the *c* axis. Inset: ferroelectric hysteresis loops measured at 100 and 128 K.

3.3 [Cu(HDABCO)(H_2O)Cl_3] (10)

In addition to the ability to form bistable N−H···N hydrogen bonds,[38,39] the order−disorder transformations of DABCO are also frequently utilized in arousing the paraelectric-to-ferroelectric phase transitions.[54,55] With a globular shape, furthermore, the highly symmetrical DABCO can also serve as a molecular rotator. Thus [Cu(HDABCO)(H_2O)Cl_3] (**10**) was synthesized as a rotator-stator-type ferroelectric in which the $[HDABCO]^+$ part acts as a rotator and the $[Cu(H_2O)Cl_3]^-$ is the stator.[56] Naturally, the paraelectric-to-ferroelectric phase transition is firstly recognized by a prominent dielectric anomaly at T_c = 235 K with a peak value of 24 at 1 MHz (Fig. 15a). Also, the temperature-dependent SHG signal implies the symmetry breaking

from the centrosymmetric phase above T_c to the noncentrosymmetric phase below T_c (Fig. 15b). Accompanying the phase transition, the symmetry breaking process with an Aizu notation of *mmmFmm*2 is just the same as that found in compounds **6** and **7**, *i.e.* from *Pnma* in the paraelectric phase above T_c to $Pna2_1$ in the ferroelectric phase below T_c. With respect to the $[Cu(HDABCO)(H_2O)Cl_3]$ units in both phases, the Cu^{2+} ion is five-coordinated by one N atom from the $[HDABCO]^+$ cation, one O atom from the H_2O molecule and three Cl^- anions, adopting a distorted trigonal-bipyramidal geometry (Fig. 16). In the paraelectric phase, the intramolecular mirror symmetry of $[Cu(HDABCO)(H_2O)Cl_3]$ unit is superimposed by the crystallographic mirror plane perpendicular to the *b* axis, fulfilling the centrosymmetry. The $[HDABCO]^+$ rotator shows twist motion around the N···N axis. In the ferroelectric phase, the freezing of such motion arouses the destruction of symmetry elements like inversion center and mirror plane, thus giving rise to a noncentrosymmetric structure. Hence the ordering of the twist motion of $[HDABCO]^+$ rotator which induces the movement from the equilibrium position is considered as the source of the symmetry-breaking phase transition and the ferroelectricity.

On the basis of the result of pyroelectric analysis, as the temperature is lowered, the P_s is vanishing above T_c and then increases to a saturation value below T_c (Fig. 15b), manifesting the paraelectric and ferroelectric phases, respectively. The comparison of the linear and nonlinear P–E curves recorded at 33 Hz provides a direct proof of the paraelectric-to-ferroelectric phase transition (Fig. 15a). Drawn from the ferroelectric hysteresis loop, the P_s is approximately 0.12 μC cm^{-2}.

Above all, a disordered room-temperature phase with severe molecular dynamics could be considered as a paraelectric phase. In view of the Curie symmetry principle, we can search for the ferroelectric phase below room temperature. A decrease in

temperature will slow down the molecular motions and lead to an ordered state with a lower symmetry. As a result of this process involving the generation or reorientation of dipole moments, the ferroelectricity is produced in the low-temperature polar phase. Meanwhile, the significant anomalies in the temperature dependence of dielectric constant and SHG coefficient are particularly helpful to detect such order-disorder type ferroelectrics.

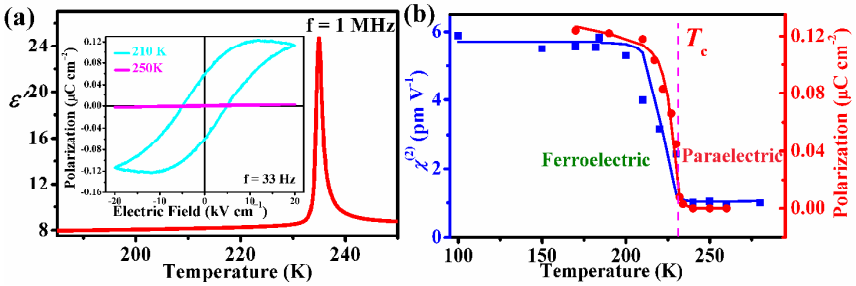

Fig. 15 (a) Temperature-dependent ε' along the c axis of **10**. Inset: ferroelectric hysteresis loops measured at 210 and 250 K. (b) Temperature dependence of $\chi^{(2)}$ and spontaneous polarization.

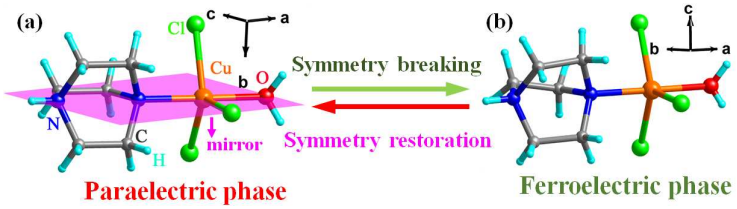

Fig. 16 Molecular structures of **10**: symmetry breaking from (a) the high-temperature paraelectric phase to (b) the low-temperature ferroelectric phase.

4 Organo–metal halide perovskite-type ferroelectrics

Hybrid organic–inorganic materials, especially those halide organo–inorganic hybrid perovskite-like compounds, integrate advantages of organic and inorganic components within a single molecular composite.[57,58] The electronic band structures of them can be easily tuned over a wide range of energy by controlling the dimensionalities of the inorganic frameworks or by modifying the halogen and/or the

organic ions, to achieve excellent electronic and photoluminescent properties. It makes these hybrid materials great candidates for the applications in optoelectronic devices, such as thin-film field-effect transistors and electro-luminescent devices.[59] $CH_3NH_3PbI_3$, as a representative, has been used in solution-processable photovoltaic devices recently with a power conversion efficiency as high as 20%.[60,61] Besides, hybrid halometallates are also structurally suitable for exploring ferroelectricity. With regard to these cases, the relatively free organic ammonium cations occupying the cavities enclosed by the MX_6 octahedra play as a key element in the design of molecular ferroelectrics. Enlightened by these, several well-designed organic–inorganic perovskite ferroelectrics exhibiting attractive phase transition properties and diverse structures are presented herein, offering a deeper insight into the relationship between symmetry breaking and ferroelectricity as well other functional properties.

4.1 One-dimensional (1D) AMX_3 perovskite-like ferroelectrics

In consideration of the fact that the order-disorder motions are one of the major sources of ferroelectricity, the flexible organic ammonium cations like the highly symmetrical cyclic ones are chosen to construct perovskite-like ferroelectrics. And, benefiting from the tunability of the organic−inorganic hybrid structures, either the ferroelectricity or the attendant physical properties can be rationally adjusted by structural modifications. Recently, a series of hexagonal stacking perovskite-like ferroelectrics with a general formula AMX_3 (A = organic cyclic ammonium, M = bivalent metal ion, and X = Cl^-, Br^-) has been developed by Xiong *et al*.[62−66] Among them, [pyrrolidinium][$MnBr_3$] (**11**),[62] [pyrrolidinium][$MnCl_3$] (**12**)[63] and [3-pyrrolinium][$MnCl_3$] (**13**)[64] were found to show photoluminescence quantum yields (PLQY) in the range of 28−56% (Scheme 6). The PLQY in these compounds are dramatically high in comparison of the traditional rare-earth-doped ferroelectrics,

providing a successful approach to integration of ferroelectricity and luminescence in organic−inorganic AMX_3-type compounds.

Despite the minor structural modifications, these analogues not only adopt analogous crystal structures but also reflect similar phase transition properties, particularly compounds **11** and **12**. At room temperature, compounds **11** and **12** crystallize in the paraelectric space group *Cmcm* (nonpolar point group *mmm* (D_{2h})), whereas compound **13** adopts a ferroelectric space group $Cmc2_1$ (polar point group *mm*2 (C_{2v})). According to the Curie symmetry principle, the ferroelectric phases of compounds **11**, **12** and the paraelectric phase of compound **13** should exist below and above room temperature, respectively. To test the above argument, the dielectric measurements were performed on compounds **11**, **12** and **13**. As a general feature of the ferroelectric phase transitions, the three complexes show prominent dielectric anomalies along the *c* axis at T_c = 219, 295 and 376 K, respectively (Fig. 17a). The abnormal ε' values near T_c are about 6500 for **11**, 4000 for **12** and 2000 for **13** at 1 MHz. Evidently, by modifying the organic component and the halogen, the Curie temperatures of the three Mn-based luminescent ferroelectrics are substantially increased to promote the practical applications. The higher T_c in **13** may result from the higher rigidity of aromatic ring.

For all three compounds, the ferroelectric space group $Cmc2_1$ falls into the maximal non-isomorphic subgroups of the paraelectric space group *Cmcm*, that is, *Ama*2, *Amm*2, $Cmc2_1$, $C222_1$, $C2/c$, $C2/m$ and $P2_1/m$. Hence the Curie symmetry principle is obeyed. The symmetry breaking process with an Aizu notation of *mmmFmm*2 is illustrated in Scheme 7, where the symmetry elements decrease from eight (E, C_2, $2C'_2$, i, σ_h, $2\sigma_v$) in the paraelectric point group *mmm* (D_{2h}) to four (E, C_2, $2\sigma_v$) in the ferroelectric point group *mm*2 (C_{2v}). The destruction of inversion center (i) is reflected

in the temperature-dependent SHG response, as the zero value above T_c and the saturated value below T_c are corresponded to the centrosymmetric paraelectric phase and noncentrosymmetric ferroelectric phase, respectively (Fig. 17b). Unsurprisingly, the temperature dependence of P_s derived from the pyroelectric effect is in coincidence with that of the SHG response, which infers a paraelectric-to-ferroelectric phase transition following the Landau phenomenological theory (Fig. 17b).

How does the inversion symmetry breaking happen? As shown in Fig. 18, the heterocyclic cations are located in the cavities between the infinite chains of 1D face-sharing MnX_6 ($X = Cl^-$ and Br^-) octahedra arranged along the *c* axis. Comparing with the insignificant transformation of the anionic chain, the order−disorder transition of the heterocyclic cation makes an essential contribution to the ferroelectric phase transition. In the paraelectric phase above T_c, the N atom and one adjacent C atom of the cation are equally distributed between two sites and can't be distinguished from each other. As a result, the disordered cationic ring is located at the 2*mm* symmetry site. In other words, the mirror planes parallel to the respective *ab*, *bc* planes and the twofold screw axis along the *b*-axis direction are superimposed by the intramolecular mirror symmetry of the cationic ring. In the ferroelectric phase below T_c, the cation proves to be ordered while the C and N atoms were refined with a single site, and thus the mirror symmetry (σ_h) perpendicular to the ring plane and the inversion symmetry (*i*) are broken. Because of the order−disorder behavior of the cation, the N atom exhibits a remarkable shift along the *c* axis, appearing as the origin of the ferroelectricity.

During the transition from the paraelectric phase to the ferroelectric phase, the *P*−*E* relationship alters from linear above T_c to nonlinear below T_c, in good agreement with the symmetry breaking (Fig. 17a). On account of the saturated ferroelectric

hysteresis loops at 50 Hz, the experimental values of P_s are obtained as high as 6 μC cm^{-2} for **11**, 5.5 μC cm^{-2} for **12** and 6.2 μC cm^{-2} for **13**. It is reasonable to expect that [3-pyrrolinium][$MnBr_3$] should be a ferroelectric, too.

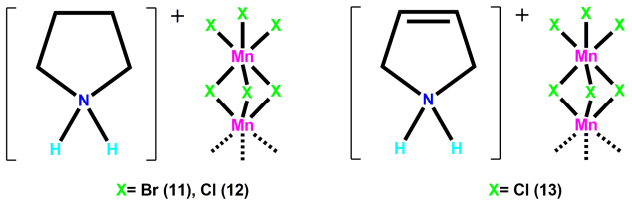

Scheme 6 Schematic structures of compounds **11**, **12** and **13**.

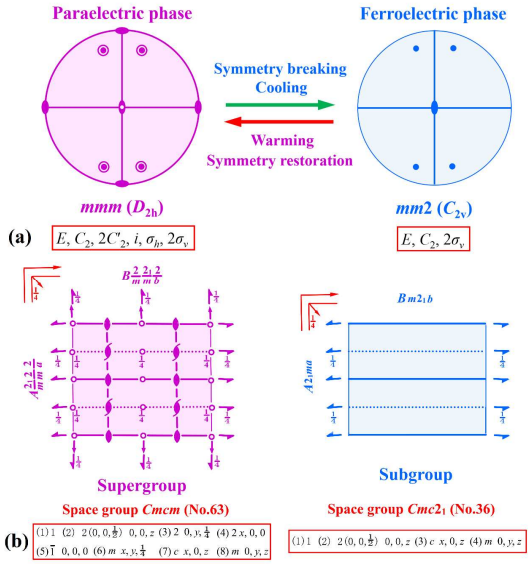

Scheme 7 Symmetry breaking occurs with an Aizu notation of *mmmFmm*2 in compounds **11**, **12** and **13**. (a) Equatorial plane projection of point groups *mmm* (D_{2h}) in the paraelectric phase and *mm*2 (C_{2v}) in the ferroelectric phase. (b) Spatial symmetry operations of the space groups *Cmcm* in the paraelectric phase and *Cmc*2$_1$ in the ferroelectric phase.

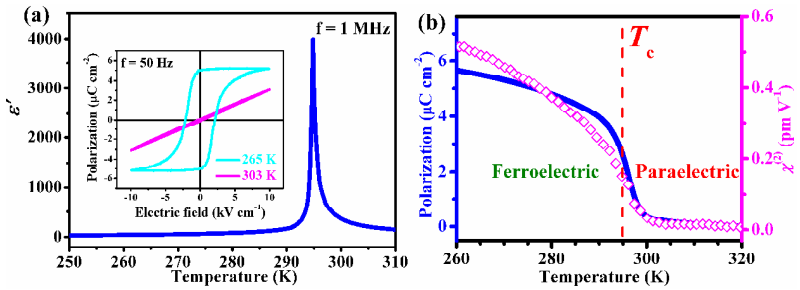

Fig. 17 (a) Temperature-dependent ε' along the *c* axis of **12**. Inset: ferroelectric hysteresis loops measured at 265 and 303 K. (b) Temperature dependence of $\chi^{(2)}$ and spontaneous polarization.

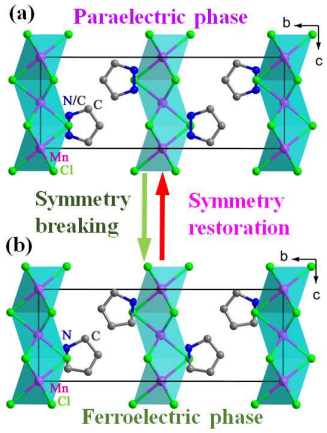

Fig. 18 Crystal structures of **12**: symmetry breaking from (a) the high-temperature paraelectric phase to (b) the low-temperature ferroelectric phase.

Comparing **12** with **13**, it is obvious that the T_c and P_s can be dramatically improved by modification of the organic cation. On the premise of unchanged cation, there is also a huge possibility that replacing the Mn ion by other transition metal ions would maintain the ferroelectricity. For this reason, [3-pyrrolinium][$CdCl_3$] (**14**)[65] and [cyclopentyl-aminium][$CdCl_3$] (**15**)[66] were synthesized as two room-temperature molecular ferroelectrics with 1D face-sharing $CdCl_6$ octahedral configuration alike to the three Mn-based complexes described above. In **14**, the phase transition mechanism and symmetry breaking are similar to those in **13**, as the space group transforms from *Cmcm* above T_c = 316 K to $Cmc2_1$ below T_c. Accompanying the ferroelectric phase transition, the broken of inversion symmetry is confirmed by the temperature-dependent SHG response (Fig. 19a). In terms of the Landau phenomenological theory, after normalization, the two curves of the temperature-dependent P_s and SHG signal should be overlapped. This is indeed the case in **14**, as displayed in Fig. 19a, indicating the appearance of symmetry breaking in a classic

proper ferroelectric. Owing to the ferroelectric phase transition, it is along the *c* axis that a great anomaly of the temperature-dependent ε' happens and reaches a high value of about 3500 at 1 MHz (Fig. 19b). Additionally, the *P*−*E* curve demonstrates a linear behavior in the paraelectric phase (Fig. 19b). Upon cooling, the nonlinear *P*−*E* relationship emerges as a fine ferroelectric hysteresis loop, which is a sign of ferroelectricity resulting from the symmetry breaking. The P_s reaches about 5.1 μC cm^{-2} at 50 Hz.

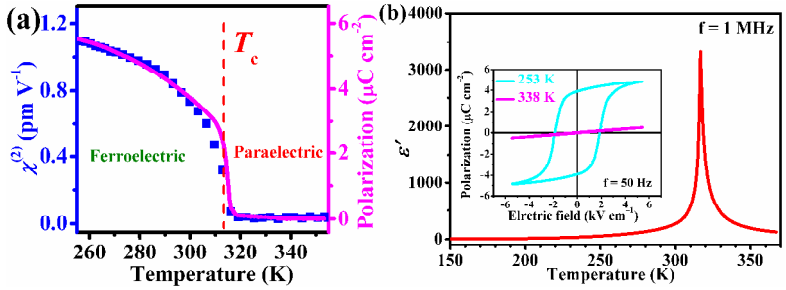

Fig. 19 (a) Temperature dependence of $\chi^{(2)}$ and spontaneous polarization of **14**. (b) Temperature-dependent ε' along the *c* axis. Inset: ferroelectric hysteresis loops measured at 253 and 338 K.

The situation in **15** is somewhat different. It undergoes a ferroelectric phase transition at T_c = 300 K. The crystal structure in the paraelectric phase above T_c adopts a centrosymmetric space group *Cmcm* (nonpolar point group *mmm* (D_{2h})), while the ferroelectric phase below T_c belongs to a noncentrosymmetric space group *Cc* (polar point group *m* (C_{1h})). *Cc* is a subgroup of *C*2/*c*, and *C*2/*c* is a subgroup of *Cmcm*, in agreement with the Curie symmetry principle. Due to the order−disorder transition of the cyclopentylaminium cation, the symmetry elements decrease from eight (E, C_2, $2C'_2$, i, σ_h, $2\sigma_v$) in the paraelectric point group *mmm* (D_{2h}) to two (E, σ_h) in the ferroelectric point group *m* (C_{1h}) with an Aizu notation of *mmmFm* (Scheme 8). It is the step-like change recorded by the temperature-dependent SHG signal that points to the inversion symmetry breaking (Fig. 20). The temperature dependence of

P_s integrated from the pyroelectric current follows almost the same path as the SHG signal, while the P_s becomes saturated at about 1.75 μC cm^{-2}. Moreover, along the *c* axis, the dielectric anomaly achieves a maximum of about 75 at 1 MHz near T_c, indicating the paraelectric-to-ferroelectric phase transition (Fig. 20).

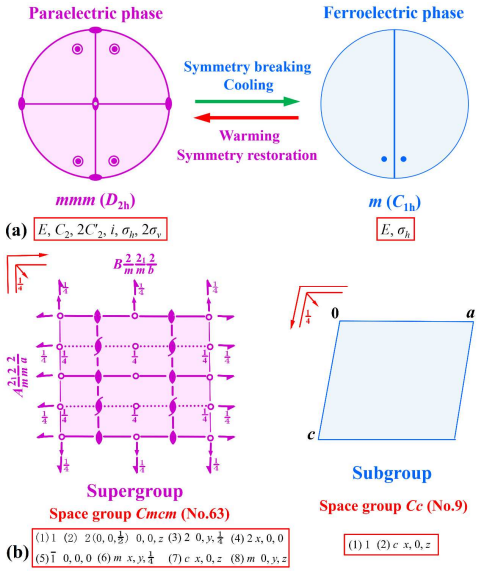

Scheme 8 Symmetry breaking occurs with an Aizu notation of *mmmFm* in **15**. (a) Equatorial plane projection of point groups *mmm* (D_{2h}) in the paraelectric phase and *m* (C_{1h}) in the ferroelectric phase. (b) Spatial symmetry operations of the space groups *Cmcm* in the paraelectric phase and *Cc* in the ferroelectric phase.

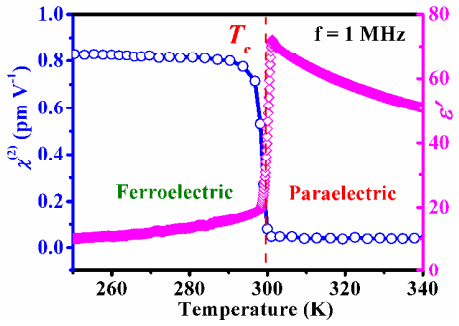

Fig. 20 Temperature dependence of $\chi^{(2)}$ and ε' along the *c* axis of **15**.

4.2 Two-dimensional (2D) layered perovskite-like ferroelectric

As distinct from the aforementioned 1D AMX_3-type perovskite-like ferroelectrics

consisting of 1D face-sharing MX_6 chains, molecular ferroelectrics with 2D layered perovskite structures are more interesting owing to the unique self-assembly and the fascinating photoelectric behavior incorporated with ferroelectricity. With a general formula of $(A\text{-}NH_3)_2MX_4$ (where A is an alkyl or aromatic moiety, M is a divalent metal ion, and X is a halogen), such structures are ideal quantum wells with anionic layers of MX_4^{2-} separated by organic cations, while the adjacent layers are held together by weak van der Waals forces. Consequently, $[benzylammonium]_2[PbCl_4]$ (**16**)[67] causes our attention, as its crystal structure at room temperature is noted as a ferroelectric $Cmc2_1$ (polar point group $mm2$ (C_{2v})) in the Cambridge Structure Database (the reference code is HORFAV).

On the basis of the Curie symmetry principle, the high-temperature paraelectric phase will adopt one of the minimal non-isomorphic supergroups of $Cmc2_1$ involving *Cmcm, Cmca*, $P6_3cm$ and $P6_3mc$. The noteworthy dielectric anomaly with a peak value of about 600 reveals the ferroelectric phase transition at around T_c = 438 K (Fig. 21a). The temperature-dependent SHG response consistent with the variation tendency of P_s shows a jump from zero above T_c to a detectable value below T_c, revealing the occurrence of inversion symmetry breaking (Fig. 21b).

During the phase transition process, the infinite layers of corner-sharing $PbCl_6$ octahedra occupying the mirror plane parallel to the *bc* plane remain almost unchanged (Fig. 22). In contrast, an obvious modification was observed in the arrangement of the benzylammonium cation, which is thought to be the main driving force of the ferroelectric phase transition. In the paraelectric phase, the benzylammonium cation with twofold orientational disorder is located at the twofold screw axis perpendicular to the *bc* plane. When the temperature decreases, only one of the two orientations perseveres in the ferroelectric phase, causing the loss of inversion

center (*i*) and the twofold screw axes (C'_2) along the *a*-, *b*-axis directions. As predicted, the phase transition is accompanied by the symmetry breaking from a centrosymmetric space group *Cmca* (point group *mmm* (D_{2h})) above T_c to a noncentrosymmetric $Cmc2_1$ below T_c. With an Aizu notation of *mmmFmm*2, the symmetry elements decrease from eight (E, C_2, $2C'_2$, i, σ_h, $2\sigma_v$) in the paraelectric point group *mmm* (D_{2h}) to four (E, C_2, $2\sigma_v$) in the ferroelectric point group *mm*2 (C_{2v}) (Scheme 9).

The motion or reorientation of the benzylammonium cation creates the P_s along the *c* axis. By the perfect ferroelectric hysteresis loop at 50 Hz, the saturated P_s is about 13 μC cm^{-2} (Fig. 21a), which is much higher than most of the reported molecular ferroelectrics. It is worth noting that, compound **16** combines the high-temperature ferroelectric property with the potential semiconducting applications.

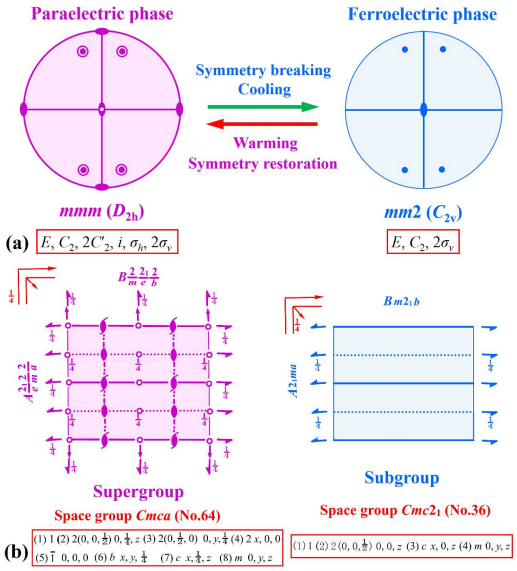

Scheme 9 Symmetry breaking occurs with an Aizu notation of *mmmFmm*2 in **16**. (a) Equatorial plane projection of point groups *mmm* (D_{2h}) in the paraelectric phase and *mm*2 (C_{2v}) in the ferroelectric phase. (b) Spatial symmetry operations of the space groups *Cmca* in the paraelectric phase and $Cmc2_1$ in the ferroelectric phase.

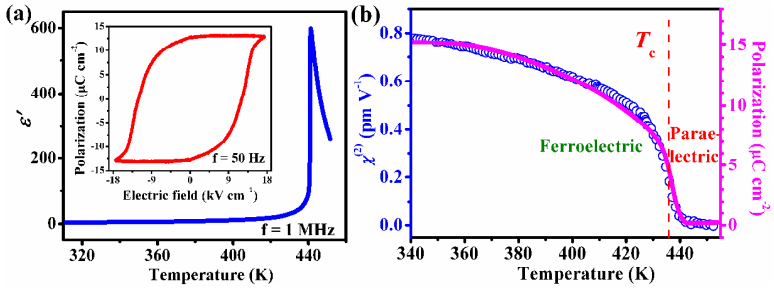

Fig. 21 (a) Temperature-dependent ε' along the *c* axis of **16**. Inset: ferroelectric hysteresis loop recorded at 383 K. (b) Temperature dependence of $\chi^{(2)}$ and spontaneous polarization.

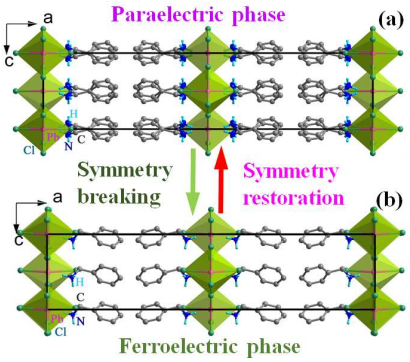

Fig. 22 Crystal structures of **16**: symmetry breaking from (a) the high-temperature paraelectric phase to (b) the low-temperature ferroelectric phase.

5 Multiple bistability in molecular ferroelectrics

Bistable materials with hysteresis loops are characterized by a physical property which can be switched from one state to another under external stimuli like heat, pressure or electric/magnetic field. Obviously, ferroelectrics are intrinsically bistable, thanks to the switchable P_s under an external electric field (*i.e.* the so-called polarization bistability). Not only that, considering the abundant physical properties like dielectric property, piezoelectricity, pyroelectricity and SHG effect related to the paraelectric-to-ferroelectric phase transition, ferroelectrics afford potential opportunities for exploring multifunctional materials with bistability in multiple physical channels. In particular, improper ferroelectrics, in which the P_s is just a

secondary order parameter, come in sight. This is because they exhibit characteristically step-like dielectric anomalies fulfilling the requirement of bistable or switchable dielectrics, distinct from the peak-like ones observed in the proper ferroelectrics.

5.1 $[Et_3MeN][FeBr_4]$ (17)

The compounds with highly symmetrical cations may easily arouse plastic phase transitions with large thermal hysteresis and thus generate bistability in multiple physical channels. However, the purely plastic phase transitions will hinder the appearance of ferroelectricity. In order to achieve bistable ferroelectric materials, one ethyl group of the highly symmetrical tetraethylammonium cation is replaced by a methyl to reduce the symmetry. Consequently, triethylmethylammonium tetrabromoferrate (III) ($[Et_3MeN][FeBr_4]$ (**17**)), is reported as a fantastic example of potential above-room-temperature molecular multiferroics with multiple bistable physical properties.[68]

At room temperature, **17** crystallizes in a noncentrosymmetric space group $P6_3mc$ (polar point group $6mm$ (C_{6v})) having eight symmetry elements (E, C_2, $2C_6$, $2C_3$, $3\sigma_v$, $3\sigma_d$), designated as the ferroelectric phase. As long as there is a paraelectric phase, it should be found at high temperature and with a higher symmetry. In the light of the temperature-dependent $\chi^{(2)}$, symmetry breaking occurs approaching T_c = 360 K, while the ferroelectric phase without inversion symmetry is SHG-active below T_c. And, the SHG-inactive state above T_c is corresponded to the centrosymmetric paraelectric phase (Fig. 23a). The ferroelectricity of **17** is suggested by the observation of a pyroelectric current below T_c. As of result of integrating the pyroelectric effect, the sharp variation of the P_s as a function of temperature is consistent with that of $\chi^{(2)}$, inferring a paraelectric-to-ferroelectric phase transition (Fig. 23a). Moreover, deduced

from the Curie symmetry principle and the SHG response, the paraelectric space group should belong to the centrosymmetric point group 6/*mmm* (D_{6h}). Therefore, the symmetry breaking process occurs with an Aizu notation of 6/*mmmF*6*mm*. Due to the extreme difficulty in obtaining the crystal structure in the paraelectric phase, however, the spatial symmetry operations are not provided here.

In addition to the paraelectric-to-ferroelectric phase transition, a magnetic phase transition also occurs at around T_c (Fig. 23b). A study of the temperature-dependent ε' with and without magnetic field points out the large coupling between magnetic ordering and ferroelectric ordering, since the ε' is greatly increased by applying a magnetic field. (Fig. 23b). Besides, the bistable ε' can be switched in two distinct states near T_c, and the step-like shape of the dramatic anomaly is common for improper ferroelectrics. Even more attractive, **17** possesses a bistable piezoelectric property at the same time, as illustrated in Fig. 23b. Triggered by the noncentrosymmetric-to-centrosymmetric phase transition, the temperature-dependent piezoelectric coefficient (d_{33}) forms a rectangular loop.

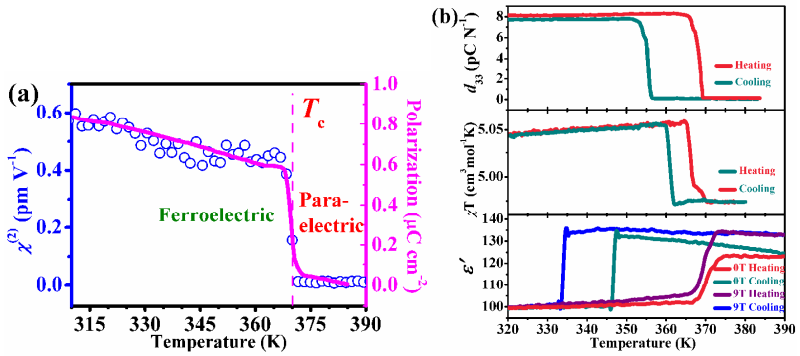

Fig. 23 (a) Temperature dependence of $\chi^{(2)}$ and spontaneous polarization of **17**. (b) Temperature dependence of piezoelectric coefficient (d_{33}), magnetic susceptibility (χT) along the *a* axis, ε' at 300 kHz with (9T) or without magnetic field (0T).

5.2 [Im]IO_4 (18)

Imidazolium perchlorate has been reported as an excellent molecular ferroelectric

with the relatively high P_s and T_c, in which the origin of ferroelectricity is ascribed to the order−disorder transformation of molecular structure.[69-71] As its analogue, imidazolium periodate ([Im]IO_4 (**18**)) is a new improper molecular ferroelectric undergoing a paraelectric-to-ferroelectric phase transition at T_c = 310 K with a large thermal hysteresis.[72] It demonstrates bistable properties in the three channels of dielectric property, piezoelectricity and SHG effect simultaneously. The reason that imidazolium perchlorate is not a bistable material might be the nonexistence of thermal hysteresis, resulting from the size of perchlorate anion smaller than the periodate anion.

Compound **18** adopts a centrosymmetric space group $P2_1/m$ in the paraelectric phase above T_c. Three C atoms and two N atoms of the $[Im]^+$ ring are indistinguishable and uniformly distributed over six apexes of the hexagon, while the center of it occupies an inversion center and the twofold screw axis along the *b*-axis direction (Fig. 24). The ordered IO_4^- anion locates at a mirror plane with two I–O bonds. Below T_c, the $[Im]^+$ cation becomes ordered as the C and N atoms can be well distinguished, and the IO_4^- anion deviates slightly from the mirror plane. Hence, the symmetry elements of mirror plane and inversion center are broken, leading to a noncentrosymmetric space group $P2_1$ in the ferroelectric phase. The symmetry breaking process with an Aizu notation of 2/*m*F2 is already given in Scheme 1, as found in compounds **1** and **2**.

For the purpose of identifying the ferroelectricity of **18**, the *P*−*E* curves were measured at different temperatures at 50 Hz as shown in Fig. 25a. Above T_c, the relationship between *P* and *E* is linear, indicating the paraelectric phase. As symmetry breaking occurs, the nonlinear *P*−*E* loop below T_c is due to the formation of the ferroelectric phase with a P_s of about 3.5 μC cm^{-2}. Given the unchanged phase

transition temperature of deuterated compound and the negligible anionic distortion, the ferroelectricity of **18** is believed to be governed by the order−disorder transformation of the $[Im]^+$ cation.

Particularly, it is the simultaneous bistability in multiple channels of SHG, dielectric, piezoelectric and ferroelectric that makes **18** highly competitive among modern materials. That is, triggered by temperature, SHG effect, dielectric constant and piezoelectric coefficient can be tuned in two distinct states and be switched by the reversible phase transition with an impressive thermal hysteresis, forming rectangular loops in the temperature range of 300–310 K. To be specific, the symmetry breaking leads to a perfect switch between SHG-off state above T_c and SHG-on state below T_c, which is crucial for photo-switching. (Fig. 25b). The switchable or bistable dielectric property is induced by the change between the ordered and disordered states of the cation, providing a possible strategy for the design of molecular switchable dielectrics. (Fig. 25b). With regard to the piezoelectric property (see Fig. 25b), the temperature dependence of d_{33} can also be switched between the piezoelectric-active and piezoelectric-inactive states. To sum up, improper moleular ferroelectrics are promising cadicates for intergrating multiple physical bistability, which open up a new avenue for applications of molecular ferroelectrics in smart devices.

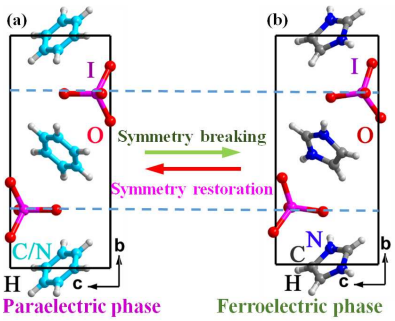

Fig. 24 Crystal structures of **18**: symmetry breaking from (a) the high-temperature paraelectric phase to (b) the low-temperature ferroelectric phase.

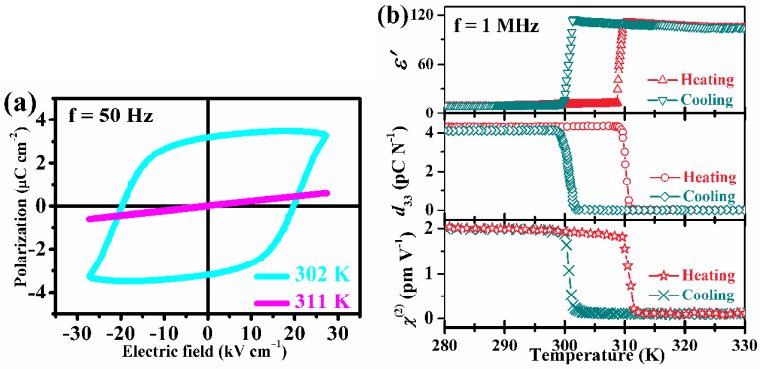

Fig. 25 (a) Ferroelectric hysteresis loops of **18** recorded at 302 and 311 K. (b) Temperature dependence of ε' along the *b* axis, d_{33} and $\chi^{(2)}$.

6 Conclusions

In conclusion, the Cambridge Structure Database collects innumerable compounds with various crystal structures, while a number of new compounds continue to spring up. To distinguish ferroelectrics among them is definitely a huge task. How to avoid blindness and detours? Experience tells us that taking advantages of the Curie symmetry principle and the Neumann's principle can make such identification quick and efficient, especially for predicting ferroelectrics on the basis of Cambridge Structure Database. Because the Curie symmetry principle contributes to the construction of the group-to-subgroup relationship between the paraelectric and ferroelectric phases, and the Neumann's principle defines the connection between the macroscopic physical properties and the macroscopic symmetries of crystals.

If a certain compound crystallizes in one of the 10 polar point groups at room temperature, the temperature-dependent dielectric constant (ε) should be measured in the temperature range of room temperature to below the melting point. For the case that no dielectric anomaly is observed, this compound will be judged as a piezoelectric or pyroelectric rather than a ferroelectric initially. Otherwise, for a prominent dielectric anomaly with at least a twofold increase, the possibility of a

high-temperature paraelectric-to-ferroelectric phase transition should not be ignored. The next step involves identifying the crystal structures above and below the phase transition temperature. At this point, the temperature dependence of $\chi^{(2)}$ is very helpful for probing the symmetry breaking and ferroelectricity. If the phase transition falls into one of the 88 species of paraelectric-to-ferroelectric types, additional physical measurements including ferroelectric hysteresis loop will be performed to confirm the ferroelectricity. Another case is the room-temperature phase adopts a paraelectric point group and displays noticeable molecular dynamics, being considered as a disordered state. With a drop in temperature, the disorder-to-order transition may cause dipole moment as well low-temperature ferroelectricity. The ferroelectric phase below room temperature can be characterized in much the same way as described above, that is, by the use of the temperature dependence of $\chi^{(2)}$ and ε. Certainly, there are exceptions to every rule. For instance, the aforementioned approach no longer serves the ferroelectrics with no Curie temperatures. Thankfully, however, with the help of piezoresponse force microscopy (PFM), the polarization switching and the ferroelectric domains can be directly observed in this class of ferroelectrics.

Once the target compound proves to be a either high-temperature or low-temperature ferroelectric, using it as a template, the ferroelectrics in this family can be enriched by molecular modifications or molecular tailoring. Consequently, such targeted searching of molecular ferroelectrics will significantly promote their applications in molecular recognition, domain engineering, molecular catalysis and biocompatible electric devices. Making full use of the advantages of these molecular materials, including light weight, softness, simple process, energy saving, biocompatible and easy film production, establishes the role of molecular ferroelectrics in the high technology industries such as aviation.[73,74] More

significantly, in view of the structural tunability in molecular ferroelectrics, the conductance and the light absorbing capacity of visible light are also adjustable, showing enormous application potential in the field of photovoltaic. All of these experiments are closely attached to the occurrence of symmetry breaking during the phase transition process.

Acknowledgement

This work was supported by 973 project (Grant2014CB932103) and the National Natural Science Foundation of China (Grants 21290172, 91422301, and 21427801).

References

1 R. C. Powell, *Symmetry, Group Theory, and the Physical Properties of Crystals*, Springer, Heidelberg, 2010.

2 M. Lax, *Symmetry Principles in Solid State and Molecular Physics*, Wiley, New York, 1974.

3 R. S. Knox and A. Gold, *Symmetry in the Solid State*, W. A. Benjamin, New York-Amsterdam, 1964.

4 G. Burns and A. M. Glazer, *Space Groups for Solid State Scientists*, Elsevier, Amsterdam, 2013.

5 R. R. Birss, *Symmetry and Magnetism*, North-Holland, Amsterdam, 1964.

6 R. E. Newnham, *Properties of Materials: Anisotropy, Symmetry, Structure*, Oxford University Press, New York, 2005.

7 V. K. Wadhawan, *Introduction to Ferroic Materials*, Gordon and Breach Science Publisher, Amsterdam, 2000.

8 H. Schmid, *J. Phys.: Condens. Matte*r, 2008, **20**, 434201.

9 M. E. Lines and A. M. Glass, *Principles and Applications of Ferroelectrics and Related Materials*, Clarendon Press, Oxford, 1977.

10 G. A. Smolenskii, V. A. Bokov, V. A. Isupov, N. N. Krainik, R. E. Pasinkov and I. A. Sokolov, *Ferroelectrics and Related Materials*, Gordon and Breach Science Publisher, New York, 1984.

11 T. Mitsui, I. Tatsuzaki, E. Nakamura, *An Introduction to the Physics of Ferroelectrics*, Gordon and Breach Science Publishers, New York, 1976.

12 N. A. Spaldin, M. Fiebig and M. Mostvoy, *J. Phys.: Condens. Matter*, 2008, **20**, 434203.

13 H. Schmid, *Ferroelectrics*, 2001, **252**, 41−50.

14 D. B. Litvin, *Acta Crystallorg. A*, 2008, **64**, 316−320.

15 J. F. Scott, *Ferroelectric Memories*, Springer, Berlin, 2000.

16 J. F. Scott, *Science*, 2007, **315**, 954−959.

17 Z. G. Ye, *Handbook of Advanced Dielectric, Piezoelectric and Ferroelectric Materials: Synthesis, Properties and Applications*, Woodhead Publishing, Cambridge, 2008.

18 J. Valasek, *Phys. Rev.*, 1920, **15**, 537−538.

19 T. Hang, W. Zhang, H. Y. Ye and R. -G. Xiong, *Chem. Soc. Rev.*, 2011, **40**, 3577−3598.

20 W. Zhang and R. -G. Xiong, *Chem. Rev.*, 2012, **112**, 1163−1195.

21 S. Horiuchi and Y. Tokura, Nat. Mater., 2008, **7**, 357−366.

22 J. F. Nye, *Physical Properties of Crystals: Their Representation by Tensors and Matrices*, Oxford University Press, New York, 2000.

23 H. Grimmer, *Ferroelectrics*, 1994, **161**, 181−189.

24 Pyroelectric coefficient (p_i) vanishes in the 11 centrosymmetric point groups (*i.e.* $\bar{1}$ (C_i), 2/*m* (C_{2h}), *mmm* (D_{2h}), 4/*m* (C_{4h}), 4/*mmm* (D_{4h}), $\bar{3}$ (C_{3i}), $\bar{3}m$ (D_{3d}), 6/*m* (C_{6h}), 6/*mmm* (D_{6h}), $m\bar{3}$ (T_h), $m\bar{3}m$ (O_h)): as a first rank polar tensor, under a

symmetry operation denoted by the transformation matrix a_{ij}, the transformation rule of p_i is $p_i' = a_{ij}p_j$, $(i, j = 1, 2, 3)$, where p_i' and p_j are the tensor components in the new and old systems, respectively. So for the inversion center,

$$p_i' = \begin{pmatrix} p_1' \\ p_2' \\ p_3' \end{pmatrix} = \begin{pmatrix} -1 & 0 & 0 \\ 0 & -1 & 0 \\ 0 & 0 & -1 \end{pmatrix} \begin{pmatrix} p_1 \\ p_2 \\ p_3 \end{pmatrix} = \begin{pmatrix} -p_1 \\ -p_2 \\ -p_3 \end{pmatrix} = -p_i .$$

According to the Neumann's principle, $p_i' = p_i$. One can conclude $p_i' = p_i = 0$.

25 Pyroelectric coefficient (p_i) vanishes in the 11 noncentrosymmetric-nonpolar point groups (*i.e.* 222 (D_2), $\bar{4}$ (S_4), 422 (D_4), $\bar{4}2m$ (D_{2d}), 32 (D_3), $\bar{6}$ (C_{3h}), 622 (D_6), $\bar{6}m2$ (D_{3h}), 23 (T), 432 (O), $\bar{4}3m$ (T_d)): for the point group 32 (D_3), under the symmetry operation of the threefold rotation axis,

$$p_i' = \begin{pmatrix} p_1' \\ p_2' \\ p_3' \end{pmatrix} = \begin{pmatrix} -1/2 & \sqrt{3}/2 & 0 \\ -\sqrt{3}/2 & -1/2 & 0 \\ 0 & 0 & 1 \end{pmatrix} \begin{pmatrix} p_1 \\ p_2 \\ p_3 \end{pmatrix} = \begin{pmatrix} -p_1/2 + \sqrt{3}p_2/2 \\ -\sqrt{3}p_1/2 - p_2/2 \\ p_3 \end{pmatrix}.$$

Then applying the symmetry operation of the twofold rotation axis,

$$p_i' = \begin{pmatrix} p_1' \\ p_2' \\ p_3' \end{pmatrix} = \begin{pmatrix} 1 & 0 & 0 \\ 0 & -1 & 0 \\ 0 & 0 & -1 \end{pmatrix} \begin{pmatrix} p_1 \\ p_2 \\ p_3 \end{pmatrix} = \begin{pmatrix} p_1 \\ -p_2 \\ -p_3 \end{pmatrix}.$$

In view of the Neumann's principle, $p_i' = p_i$, we have $p_i' = p_i = 0$. By analogy, the pyroelectricity is absent in the other noncentrosymmetric-nonpolar point groups.

26 K. Aizu, Phys. Rev. B, 1970, 2, 754−772.

27 N. E. Sherstyuka, E. D. Mishinaa, S. D. Lavrov, A. M. Buryakov, M. A. Marchenkova, A. S. Elshin and A. S. Sigov, *Ferroelectrics*, 2015, **477**, 29–46.

28 M. Fiebig, *J. Opt. Soc. Am. B*, 2005, **22**, 96−118.

29 S. A. Denev, T. T. A. Lummen, E. Barnes, A. Kumar and V. Gopalan, *J. Am. Ceram. Soc.*, 2011, **94**, 2699−2727.

30 M. Fiebig, D. Frohlich, K. Kohn, S. Leute, T. Lottermoser, V. V. Pavlov and R. V. Pisarev, *Phys. Rev. Lett.*, 2000, **84**, 5620−5623.

31 H. -L. Cai, D. -W. Fu, Y. Zhang, W. Zhang and R. -G. Xiong, *Phys. Rev. Lett.*, 2012, **109**, 169601.

32 Second-order nonlinear coefficient ($\chi^{(2)}$) vanishes in the 11 centrosymmetric point groups as well the 3 noncentrosymmetric-nonpolar point groups including 422(D_4), 622(D_6), and 432(O): the second-order nonlinear coefficient is a third rank polar property tensor represented by $\chi_{ijk}^{(2)}$, whose transformation rule under the symmetry operation with a transformation matrix a_{ij} is

$$\chi_{ijk}^{(2)\prime} = a_{il}a_{jm}a_{kn}\chi_{ilmn}^{(2)}, (i, j, k, \ldots = 1, 2, 3),$$

Where $\chi_{ijk}^{(2)\prime}$ and $\chi_{lmn}^{(2)}$ refers to the respective tensor components in the new and old systems. Under the symmetry operation of inversion center, there is, $\chi_{ijk}^{(2)\prime} = -\chi_{ijk}^{(2)}$, while based on the Neumann's principle, $\chi_{ijk}^{(2)\prime} = \chi_{ijk}^{(2)}$, so the conclusion is $\chi_{ijk}^{(2)\prime} = \chi_{ijk}^{(2)} = 0$. Also, through the relevant deduction, one can prove the absence of $\chi_{ijk}^{(2)}$ in the point groups 422(D_4), 622(D_6), and 432(O).

33 J. Grindlay, *An Introduction to the Phenomenological Theory of Ferroelectricity*, Pergamon Press, Oxford, 1970.

34 G. -C. Xu, X. -M. Ma, L. Zhang, Z. -M. Wang and S. Gao, *J. Am. Chem. Soc.*, 2010, **132**, 9588−9590.

35 G. -C. Xu, W. Zhang, X. -M. Ma, Y. -H. Chen, L. Zhang, H. -L. Cai, Z. -M. Wang, R. -G. Xiong and S. Gao, *J. Am. Chem. Soc.*, 2011, **133**, 14948−14951.

36 Z. H. Sun, T. L. Chen, J. H. Luo and M. C. Hong, *Angew. Chem. Int. Ed.*, 2012, **51**, 3871−3876.

37 S. Koval, J. Kohanoff, J. Lasave, G. Colizzi and R. L. Migoni, *Phys. Rev. B*, 2005,

71, 184102.

38 A. Katrusiak and M. Szafranski, *Phy. Rev. Lett.*, 1999, **82**, 576−579.

39 A. Katrusiak, M. Szafranski, and G. J. McIntyre, *Phy. Rev. Lett.*, 2002, **89**, 215507.

40 D. W. Fu, W. Zhang, H. L. Cai, J. Z. Ge, Y. Zhang and R. -G. Xiong, *Adv. Mater.*, 2011, **23**, 5658−5662.

41 D. W. Fu, H. L. Cai, Y. M. Liu, Q. Ye, W. Zhang, Y. Zhang, X. Y. Chen, G. Giovannetti, M. Capone, J. Y. Li and R. -G. Xiong, *Science*, 2013, **339**, 425−428.

42 H. L. Cai, W. Zhang, J. Z. Ge, Y. Zhang, K. Awaga, T. Nakamura and R. -G. Xiong, *Phys. Rev. Lett.*, 2011, **107**, 147601.

43 H. Y. Ye, Y. Zhang, S. I. Noro, K. Kubo, M. Yoshitake, Z. Q. Liu, H. L. Cai, D. W. Fu, H. Yoshikawa, K. Awaga, R. -G. Xiong and T. Nakamura, *Sci Rep-UK*, 2013, **3**, 2249.

44 H. Y. Ye, Y. Zhang, D. W. Fu and R. -G. Xiong, *Angew. Chem. Int. Ed.*, 2014, **53**, 6724−6729.

45 K. H. Weyrich, *Ferroelectrics*, 1990, **104**, 183−194.

46 K. H. Weyrich and P. Madenach, *Ferroelectrics*, 1990, **111**, 9−14.

47 C. S. Vogelsberg and M. A. Garcia-Garibay, *Chem. Soc. Rev.*, 2012, **41**, 1892−1910.

48 T. Akutagawa, H. Koshinaka, D. Sato, S. Takeda, S. -I. Noro, H. Takahashi, R. Kumai, Y. Tokura and T. Nakamura, *Nat. Mater.*, 2009, **8**, 342−347.

49 D. W. Fu, H. L. Cai, S. H. Li, Q. Ye, L. Zhou, W. Zhang, Y. Zhang, F. Deng and R. -G. Xiong, *Phys. Rev. Lett*., 2013, **110**, 257601.

50 D. W. Fu, W. Zhang, H. L. Cai, Y. Zhang, J. Z. Ge, R. -G. Xiong and S. D. Huang, *J. Am. Chem. Soc.*, 2011, **133**, 12780−12786.

51 H. Y. Ye, S. H. Li, Y. Zhang, L. Zhou, F. Deng and R. -G. Xiong, *J. Am. Chem. Soc.*, 2014, **136**, 10033−10040.

52 Y. Zhang, H. Y. Ye, D. W. Fu and R. -G. Xiong, *Angew. Chem. Int. Ed.*, 2014, **53**, 2114−2118.

53 Y. -Z. Tang, Y. -M. Yu, J. -B. Xiong, Y. -H. Tan and H. -R. Wen, *J. Am. Chem. Soc.*, 2015, **137**, 13345−13351.

54 W. Zhang, L. Z. Chen, R. -G. Xiong, T. Nakamura and S. P. D. Huang, *J. Am. Chem. Soc.*, 2009, **131**, 12544−12545.

55 W. Zhang, H. Y. Ye, H. L. Cai, J. Z. Ge, R. -G. Xiong and S. P. D. Huang, *J. Am. Chem. Soc.*, 2010, **132**, 7300−7302.

56 Y. Zhang, W. Zhang, S. H. Li, Q. Ye, H. L. Cai, F. Deng, R. -G. Xiong and S. D. Huang, *J. Am. Chem. Soc.*, 2012, **134**, 11044−11049.

57 D. B. Mitzi, C. A. Feild, W. T. A. Harrison and A. M. Guloy, *Nature*, 1994, **369**, 467−469.

58 D. B. Mitzi, K. Chondroudis and C. R. Kagan, *IBM J. Res. Dev.*, 2001, **45**, 29−45.

59 C. R. Kagan, D. B. Mitzi and C. Dimitrakopoulos, *Science*, 1999, **286**, 945−947.

60 H. Zhou, Q. Chen, G. Li, S. Luo, T. -B. Song, H. -S. Duan, Z. Hong, J. You, Y. Liu and Y. Yang, *Science*, 2014, **345**, 542−546.

61 W. S. Yang, J. H. Noh, N. J. Jeon, Y. C. Kim, S. Ryu, J. Seo and S. I. Seok, *Science*, 2015, **348**, 1234−1237.

62 Y. Zhang, W. Q. Liao, D. W. Fu, H. Y. Ye, C. M. Liu, Z. N. Chen and R. -G. Xiong, *Adv. Mater.*, 2015, **27**, 3942−3946.

63 Y. Zhang, W. Q. Liao, D. W. Fu, H. Y. Ye, Z. N. Chen and R. -G. Xiong, *J. Am. Chem. Soc.*, 2015, **137**, 4928−4931.

64 H. Y. Ye, Q. H. Zhou, X. H. Niu, W. Q. Liao, D. W. Fu, Y. Zhang, Y. M. You, J. Wang, Z. N. Chen and R. -G. Xiong, *J. Am. Chem. Soc.*, 2015, **137**, 13148−13154.

65 H. Y. Ye, Y. Zhang, D. W. Fu and R. -G. Xiong, *Angew. Chem. Int. Ed.*, 2014, **53**,

11242−11247.

66 Y. Zhang, H. Y. Ye, W. Zhang and R. -G. Xiong, *Inorg. Chem. Front.*, 2014, **1**, 118−123.

67 W. Q. Liao, Y. Zhang, C. L. Hu, J. G. Mao, H. Y. Ye, P. F. Li, S. D. Huang and R. -G. Xiong, *Nat. Commun.*, 2015, **6**, 7338.

68 H. L. Cai, Y. Zhang, D. W. Fu, W. Zhang, T. Liu, H. Yoshikawa, K. Awaga and R. -G. Xiong, *J. Am. Chem. Soc.*, 2012, **134**, 18487−18490.

69 Y. Zhang, Y. M. Liu, H. Y. Ye, D. W. Fu, W. X. Gao, H. Ma, Z. G. Liu, Y. Y. Liu, W. Zhang, J. Y. Li, G. L. Yuan and R. -G. Xiong, *Angew. Chem. Int. Ed.*, 2014, **53**, 5064–5068.

70 J. Smith and K. Mueller, *Science*, 2014, **344**, 236.

71 Z. Pająk, P. Czarnecki, B. Szafrańska, H. Małuszyńska and Z. Fojud, *J. Chem. Phys.*, 2006, **124**, 144502.

72 Y. Zhang, H. Y. Ye, H. L. Cai, D. W. Fu, Q. Ye, W. Zhang, Q. Zhou, J. Wang, G. L. Yuan and R. -G. Xiong, *Adv. Mater.*, 2014, **26**, 4515–4520.

73 J. Y. Li, Y. M. Liu, Y. H. Zhang, H. L. Cai and R. -G. Xiong, *Phys.Chem. Chem. Phys.,* 2013, **15**, 20786–20796.

74 A. S. Tayi, A. Kaeser, M. Matsumoto, T. Aida and S. I. Stupp, *Nat. Chem.*, 2015, **7**, 281–294.